Green's theorem in seismic imaging across the scales

Kees Wapenaar[1], Joeri Brackenhoff[1], and Jan Thorbecke[1]

[1]Department of Geoscience and Engineering, Delft University of Technology, Stevinweg 1, 2628 CN Delft, The Netherlands

Correspondence: Kees Wapenaar (c.p.a.wapenaar@tudelft.nl)

Abstract. The solid earth and exploration communities independently developed a variety of seismic imaging methods for passive- and active-source data. Despite the seemingly different approaches and underlying principles, many of those methods are based in some way or another on Green's theorem. The aim of this paper is to discuss a variety of imaging methods in a systematic way, using a specific form of Green's theorem (the homogeneous Green's function representation) as the common starting point. The imaging methods we cover are time-reversal acoustics, seismic interferometry, back propagation, source-receiver redatuming and imaging by double focusing. We review classical approaches and discuss recent developments that fully account for multiple scattering, using the Marchenko method. We briefly indicate new applications for monitoring and forecasting of responses to induced seismic sources, which are discussed in detail in a companion paper.

1 Introduction

Traditionally, methods for seismic imaging evolved independently in the solid earth and exploration communities. This has led to a wealth of imaging methods for passive- and active-source data, based on a variety of principles such as time-reversal acoustics, Green's function retrieval by noise correlation (also known as seismic interferometry), back propagation (also known as holography), source-receiver redatuming, and so on. According to the authors' perception, the different communities have gradually come closer together in the past fifteen years or so. In particular the advent of Green's function retrieval by noise correlation has led to a significant cross-fertilisation between the communities via jointly organised sessions and workshops, as well as special issues in journals (e.g. "Seismic Interferometry," Geophysics, July-August 2006; New developments on imaging and monitoring with seismic noise, "Comptes Rendus Geoscience," September 2011, etc.). Moreover, the fields of adjoint tomography in the solid earth community (e.g. Bozdağ et al. (2016)) and full waveform inversion in the exploration community (e.g. Virieux and Operto (2009)) appear to have much in common and nowadays much cooperation is taking place in these fields between researchers of both communities. The current special issue on "Advances in seismic imaging across the scales" is another welcome initiative to bring the solid earth and exploration communities closer together.

Many of the methods mentioned above are rooted in some way or another in Green's theorem (Green, 1828; Challis and Sheard, 2003). The current paper is a modest attempt to discuss a variety of imaging methods and their underlying principles in a systematic way, using Green's theorem as the common starting point. We are by far not the first to recognise links between different imaging methods. For example, Esmersoy and Oristaglio (1988) discussed the link between back propagation and reverse-time migration, Derode et al. (2003) derived seismic interferometry from the principle of time-reversal acoustics by

physical reasoning, Schuster et al. (2004) linked seismic interferometry to back propagation, and links between adjoint tomographic inversion methods and time-reversal acoustics have been made by Tarantola (1984) and Tromp et al. (2005), to name but a few. In this paper we restrict ourselves to linking several imaging methods, including recent developments using the 3D Marchenko method, but we refrain from discussing inversion methods.

5   Using a specific form of Green's theorem (i.e., the classical representation of the homogeneous Green's function, originally developed for optical holography (Porter, 1970; Porter and Devaney, 1982)), we derive time-reversal acoustics, seismic interferometry, back propagation, source-receiver redatuming and imaging by double focusing in a systematic way, confirming that these methods are all different sides of the same coin. We briefly discuss the potential and limitations of these methods. Because the classical homogeneous Green's function representation is based on a closed boundary integral, an implicit assumption for

10   all these methods is that the medium of interest can be accessed from all sides. Because in most seismic applications acquisition is limited to the earth's surface, a major part of the closed boundary integral is necessarily neglected. This implies that errors are introduced and, in particular, that multiple reflections between layer interfaces are not correctly handled. To address this issue, we also discuss a recently developed single-sided representation of the homogeneous Green's function. We use this to derive, in the same systematic way, modified seismic imaging methods that do account for multiple reflections between

15   layer interfaces. In a companion paper (Brackenhoff et al., 2019) we extensively discuss applications for monitoring induced seismicity.

Although the solid earth supports elastodynamic waves, to facilitate the comparison of the different methods discussed in this paper we have chosen to consider acoustic waves only. At several places we give references to extensions of the methods that account for elastodynamic waves.

20   ## 2   Theory and applications of classical wave field representations

2.1   Classical homogeneous Green's function representation

We review the classical representation of the homogeneous Green's function. We consider an inhomogeneous lossless acoustic medium, with mass density $\rho = \rho(\mathbf{x})$ and compressibility $\kappa = \kappa(\mathbf{x})$, where $\mathbf{x} = (x_1, x_2, x_3)$ denotes the Cartesian coordinate vector. In this medium we define a unit impulsive point source of volume-injection rate density $q(\mathbf{x}, t) = \delta(\mathbf{x} - \mathbf{x}_A)\delta(t)$, where

25   $\delta(\cdot)$ denotes the Dirac delta function, $\mathbf{x}_A$ the position of the source and where t stands for time. The response to this source, observed at any position $\mathbf{x}$ in the inhomogeneous medium, is the Green's function $G(\mathbf{x}, \mathbf{x}_A, t)$. It obeys the following wave equation

$$\partial_i(\rho^{-1}\partial_i G) - \kappa\partial_t^2 G = -\delta(\mathbf{x} - \mathbf{x}_A)\partial_t\delta(t), \tag{1}$$

where ∂_t stands for the temporal differential operator $\partial/\partial t$ and ∂_i for the spatial differential operator $\partial/\partial x_i$. Latin subscripts

30   (except t) take on the values 1, 2 and 3, and Einstein's summation convention applies to repeated subscripts. We impose the condition $G(\mathbf{x}, \mathbf{x}_A, t) = 0$ for $t < 0$, so that $G(\mathbf{x}, \mathbf{x}_A, t)$ is the causal solution of equation (1), propagating forward, away from
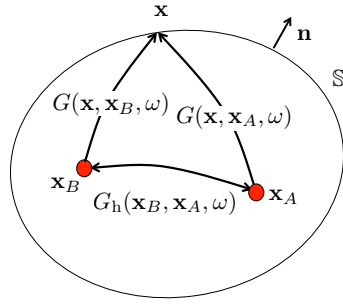
Figure 1. Configuration for the homogeneous Green's function representation (equation 6). The rays in this and subsequent figures represent the full responses between the source and receiver points, including primary an multiple scattering.

the source at $\mathbf{x}_A$. Note that the Green's function obeys source-receiver reciprocity, i.e., $G(\mathbf{x}_B,\mathbf{x}_A,t) = G(\mathbf{x}_A,\mathbf{x}_B,t)$. This property will be frequently used without always mentioning it explicitly.

The time-reversal of the Green's function, $G(\mathbf{x},\mathbf{x}_A,-t)$, is the acausal solution of equation (1), which, for $t < 0$, propagates backward, towards the point $\mathbf{x}_A$. The homogeneous Green's function $G_{\mathrm{h}}(\mathbf{x},\mathbf{x}_A,t)$ is defined as the superposition of the Green's function and its time reversal, according to

$$G_{\mathrm{h}}(\mathbf{x},\mathbf{x}_A,t) = G(\mathbf{x},\mathbf{x}_A,t) + G(\mathbf{x},\mathbf{x}_A,-t). \tag{2}$$

It obeys a homogeneous wave equation (i.e., a wave equation without a singularity at the right-hand side), hence $\partial_i(\rho^{-1}\partial_i G_{\mathrm{h}}) - \kappa\partial_t^2 G_{\mathrm{h}} = 0$. We define the Fourier transform of a space- and time-dependent function $u(\mathbf{x},t)$ as

$$u(\mathbf{x},\omega) = \int\limits_{-\infty}^{\infty} u(\mathbf{x},t)\exp(i\omega t)\mathrm{d}t. \tag{3}$$

Here ω denotes angular frequency and i the imaginary unit. For notational convenience, we use the same symbol for quantities in the time domain and in the frequency domain. The wave equation for the Green's function in the frequency domain reads

$$\partial_i(\rho^{-1}\partial_i G) + \kappa\omega^2 G = i\omega\delta(\mathbf{x} - \mathbf{x}_A). \tag{4}$$

The homogeneous Green's function in the frequency domain is defined as

$$G_{\mathrm{h}}(\mathbf{x},\mathbf{x}_A,\omega) = G(\mathbf{x},\mathbf{x}_A,\omega) + G^*(\mathbf{x},\mathbf{x}_A,\omega) = 2\Re\{G(\mathbf{x},\mathbf{x}_A,\omega)\}, \tag{5}$$

where the superscript asterisk denotes complex conjugation and where $\Re$ means that the real part is taken. The classical representation of the homogeneous Green's function reads (Porter (1970); Oristaglio (1989); supplementary material, section 1.3)

$$G_{\mathrm{h}}(\mathbf{x}_B,\mathbf{x}_A,\omega) = \oint\limits_{\mathbb{S}} \frac{1}{i\omega\rho(\mathbf{x})} \Big(\{\partial_i G(\mathbf{x},\mathbf{x}_B,\omega)\}G^*(\mathbf{x},\mathbf{x}_A,\omega) - G(\mathbf{x},\mathbf{x}_B,\omega)\partial_i G^*(\mathbf{x},\mathbf{x}_A,\omega) \Big) n_i\mathrm{d}\mathbf{x}, \tag{6}$$

see Figure 1. Here $\mathbb{S}$ is an arbitrarily shaped closed boundary with outward pointing normal vector $\mathbf{n} = (n_1, n_2, n_3)$. It is assumed that $\mathbf{x}_A$ and $\mathbf{x}_B$ are situated inside $\mathbb{S}$. Note that the aforementioned authors use a slightly different definition of

the Green's function (the factor $i\omega$ in the source term in equation (4) is absent in their case). Nevertheless, we will refer to equation (6) as the classical homogeneous Green's function representation. When the medium outside $\mathbb{S}$ is homogeneous and $\mathbb{S}$ is sufficiently smooth, this representation may be approximated by

$$G_{\mathrm{h}}(\mathbf{x}_B, \mathbf{x}_A, \omega) = -2 \oint_{\mathbb{S}} \frac{1}{i\omega\rho(\mathbf{x})} G(\mathbf{x}, \mathbf{x}_B, \omega) \partial_i G^*(\mathbf{x}, \mathbf{x}_A, \omega) n_i \mathrm{d}\mathbf{x}. \tag{7}$$

5 The main approximation is that evanescent waves are neglected at $\mathbb{S}$ (Zheng et al., 2011; Wapenaar et al., 2011). The latter representation forms the starting point for discussing a number of applications in the next sections.

2.2 Time-reversal acoustics

The field of time-reversal acoustics has been pioneered by Fink and co-workers (Fink, 1992; Derode et al., 1995; Draeger and Fink, 1999; Fink, 2006). It is based on the fact that the acoustic wave equation for a lossless medium is invariant under time
10 reversal (for discussions about elastodynamic time-reversal methods we refer to Scalerandi et al. (2009), Anderson et al. (2009) and Wang and McMechan (2015)). Hence, given a particular solution of the wave equation, its time-reversal obeys the same wave equation. Figure 2 illustrates the principle (after Derode et al. (1995) and Fink (2006)). In Figure 2a, an impulsive source at $\mathbf{x}_A$ emits a wave field which, after propagation through a highly scattering medium, is recorded by receivers at $\mathbf{x}$ on the boundary $\mathbb{S}_0$. The recordings are denoted as $v_{\mathrm{n}}(\mathbf{x}, \mathbf{x}_A, t)$, where v_{n} stands for the normal component of the particle velocity.
15 Note that these recordings are very complex due to multiple scattering in the medium. In Figure 2b, the time-reversals of these complex recordings, $v_{\mathrm{n}}(\mathbf{x}, \mathbf{x}_A, -t)$, are emitted from the boundary $\mathbb{S}_0$ into the medium. After propagating through the same scattering medium, the field should focus at $\mathbf{x}_A$, i.e., at the position of the original source. Figure 2c shows a snapshot of the field at $t = 0$, which indeed contains a focus at $\mathbf{x}_A$. Figure 2d shows a cross-section of the amplitudes at $t = 0$ at the depth level of the focus (the blue curve with the sharp peak). For comparison, when the same field $v_{\mathrm{n}}(\mathbf{x}, \mathbf{x}_A, -t)$ propagates from $\mathbb{S}_0$
20 through a homogeneous medium to $\mathbf{x}_A$, hardly any focusing takes place (Figure 2d, green curve without a well-defined peak). Hence, we can conclude that multiple scattering contributes to the formation of the focus in Figure 2c. As a matter of fact, the scattering medium effectively widens the aperture angle, meaning that the resolution of the focus is even better than when the scatterers would be absent in both steps of the experiment (the latter represented by the red curve in Figure 2d).

The time-reversal principle can be made more quantitative using Green's theorem (Fink, 2006). First, using the equation of
25 motion, we express the normal component of the particle velocity at $\mathbb{S}$ in the frequency domain as

$$v_{\mathrm{n}}(\mathbf{x}, \mathbf{x}_A, \omega) = \frac{1}{i\omega\rho(\mathbf{x})} n_i \partial_i G(\mathbf{x}, \mathbf{x}_A, \omega) s(\omega), \tag{8}$$

where $s(\omega)$ is the spectrum of the source at $\mathbf{x}_A$. Using this in the homogeneous Green's function representation of equation (7) we obtain

$$G_{\mathrm{h}}(\mathbf{x}_B, \mathbf{x}_A, \omega) s^*(\omega) = 2 \oint_{\mathbb{S}} G(\mathbf{x}_B, \mathbf{x}, \omega) v_{\mathrm{n}}^*(\mathbf{x}, \mathbf{x}_A, \omega) \mathrm{d}\mathbf{x}, \tag{9}$$
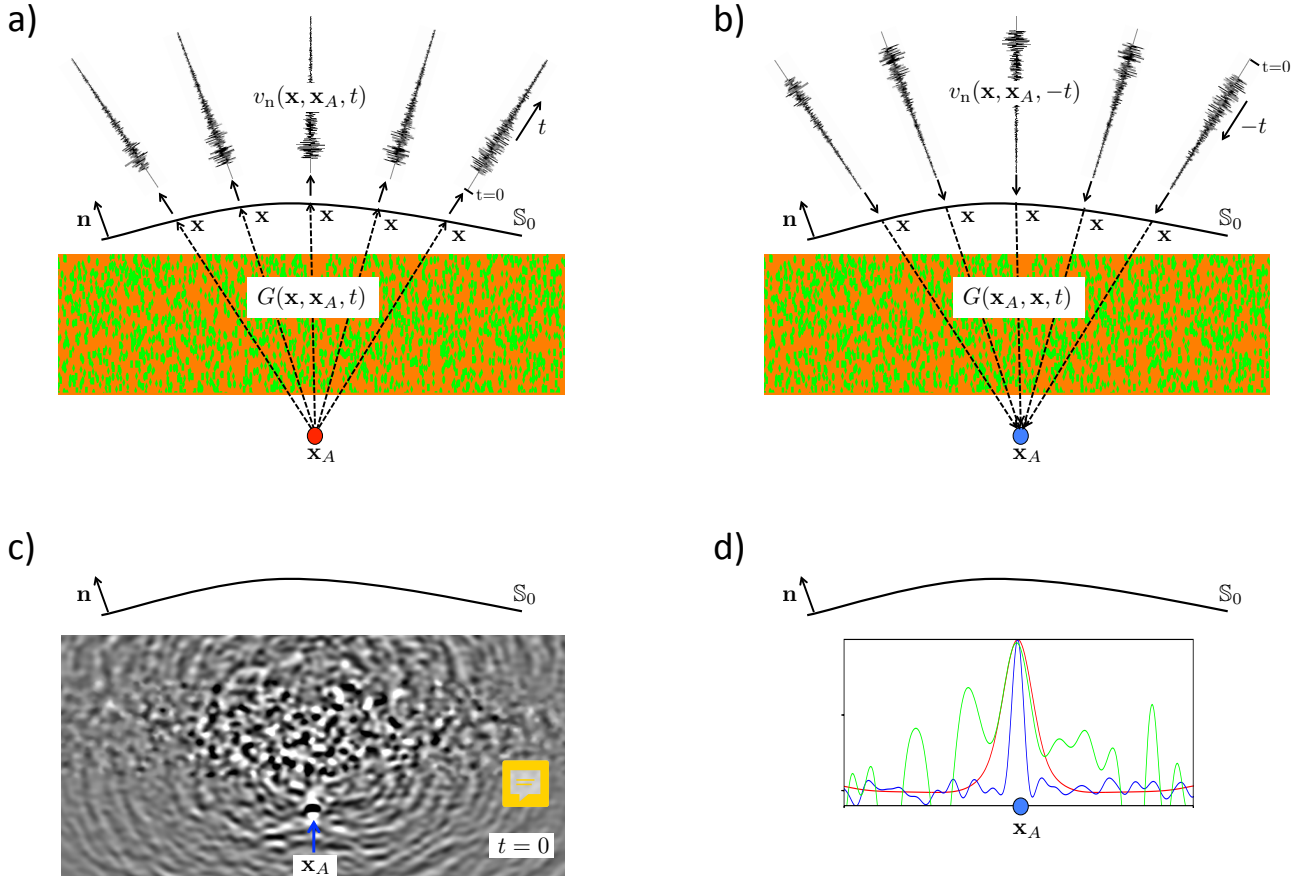
4

Figure 2. Principle of time-reversal acoustics (artist impression, figures not to scale). (a) Forward propagation from $\mathbf{x}_A$ to the surface $\mathbb{S}_0$. (b) Emission of the time-reversed recordings from $\mathbb{S}_0$ into the medium. (c) Snapshot of the wave field at $t = 0$, with focus at $\mathbf{x}_A$. (d) Amplitude cross-sections of focussed field. Blue curve: cross-section obtained from (c). Green curve: scatterers only present during forward propagation. Red curve: no scatterers in both steps.

or, in the time domain (using equation 2),

$$\{G(\mathbf{x}_B, \mathbf{x}_A, t) + G(\mathbf{x}_B, \mathbf{x}_A, -t)\} * s(-t) = 2 \oint_{\mathbb{S}} \underbrace{G(\mathbf{x}_B, \mathbf{x}, t)}_{'\text{propagator}'} * \underbrace{v_\mathrm{n}(\mathbf{x}, \mathbf{x}_A, -t)}_{'\text{source}'} \, \mathrm{d}\mathbf{x}, \tag{10}$$

where the inline asterisk ($*$) denotes temporal convolution. This is the fundamental expression for time-reversal acoustics. The right-hand side quantifies the emission of the time-reversed field $v_\mathrm{n}(\mathbf{x}, \mathbf{x}_A, -t)$ by sources at $\mathbf{x}$ on the boundary $\mathbb{S}$ and propagation of this field by the Green's function $G(\mathbf{x}_B, \mathbf{x}, t)$ through the inhomogeneous medium to any point $\mathbf{x}_B$ inside $\mathbb{S}$; the integral is taken over all sources on $\mathbb{S}$ (Huygens' principle). The left-hand side quantifies the field at any point $\mathbf{x}_B$ inside $\mathbb{S}$, which consists of a backward propagating field $G(\mathbf{x}_B, \mathbf{x}_A, -t) * s(-t)$, converging to $\mathbf{x}_A$, and a forward propagating field $G(\mathbf{x}_B, \mathbf{x}_A, t) * s(-t)$, propagating away from $\mathbf{x}_A$. By setting $\mathbf{x}_B$ equal to $\mathbf{x}_A$ we obtain the field at the focus (i.e., at the position of the original source, as illustrated by Figure 2b). By taking $\mathbf{x}_B$ variable in a small region around $\mathbf{x}_A$, while setting t equal to

zero, equation (10) quantifies the focal spot. Assuming the source function $s(t)$ is symmetric, this yields

$$[\{G(\mathbf{x}_B, \mathbf{x}_A, t) + G(\mathbf{x}_B, \mathbf{x}_A, -t)\} * s(t)]_{t=0} = -\frac{\bar{\rho}}{2\pi r}\dot{s}(r/\bar{c}) \qquad (11)$$

(Douma and Snieder, 2015; Wapenaar and Thorbecke, 2017), where $\bar{c}$ and $\bar{\rho}$ are the propagation velocity and mass density in the neighborhood of $\mathbf{x}_A$, r is the distance of $\mathbf{x}_B$ to $\mathbf{x}_A$, and $\dot{s}(t)$ denotes the derivative of the source function $s(t)$.

5   It should be noted that the integration in equation (10) takes place over sources on a closed boundary $\mathbb{S}$. However, in the example in Figure 2 the time-reversed field is emitted into the medium from a finite open boundary $\mathbb{S}_0$. Despite this discrepancy, a very good focus is obtained around $\mathbf{x}_A$. Nevertheless, Figure 2c also shows a noisy field at $t = 0$, particularly in the scattering region. According to equation (10), this noisy field would vanish when the time-reversed field would be emitted from a closed boundary.

10   Figure 2 is exemplary for ultrasonic applications of time-reversal acoustics, because in those applications it is feasible to physically emit the time-reversed field into the real medium (Fink, 1992; Cassereau and Fink, 1992; Derode et al., 1995; Draeger and Fink, 1999; Fink, 2006; Tanter and Fink, 2014). Time-reversal acoustics also finds applications in geophysics, but in those applications the time-reversed field is emitted numerically into a model of the earth. This is used for source characterization (McMechan, 1982; Gajewski and Tessmer, 2005; Larmat et al., 2010) and for structural imaging by reverse-
15   time migration (McMechan, 1983; Whitmore, 1983; Baysal et al., 1983; Etgen et al., 2009; Zhang and Sun, 2009; Clapp et al., 2010). In these model-driven applications it is much more difficult to account for multiple scattering and therefore it is usually ignored. Moreover, the scattering mechanism is often very different, particularly in applications dedicated to image the earth's crust. We discuss a second time-reversal example to illustrate this.

Whereas in Figure 2 we considered short-period multiple scattering at randomly distributed point-like scatterers in a homo-
20   geneous background medium, in Figure 3 we consider long-period multiple scattering at extended interfaces between layers with distinct medium parameters (which is exemplary for multiple scattering in the earth's crust). Figure 3a shows the response $v_{\mathrm{n}}(\mathbf{x}, \mathbf{x}_A, t)$ to a source at $\mathbf{x}_A$ inside a layered medium, observed at the surface $\mathbb{S}_0$. The time-reversal of this response is emitted from $\mathbb{S}_0$ into the same layered medium. The field at $t = 0$ is shown in Figure 3b. We observe again a clear focus at $\mathbf{x}_A$, but this time the multiple scattering does not contribute to the resolution of this focus (because no widening of the aperture angle takes
25   place). On the contrary, the multiply scattered waves give rise to strong distinct artefacts at other regions in the medium. Again, these artefacts would disappear entirely when the time-reversed field would be emitted from a closed boundary, but this is of course unrealistic for geophysical applications. In section 3.2 we discuss a modified approach to single-sided time-reversal acoustics which does not suffer from artefacts like those in Figure 3b.

2.3 Seismic interferometry

30   Under certain conditions, the cross-correlation of ambient noise recordings at two receivers converges to the response that would be measured at one of the receivers if there were an impulsive source at the position of the other. This methodology, which creates a virtual source at the position of an actual receiver, is known as Green's function retrieval, or seismic interferometry. At ultrasonic scale it has been pioneered by Weaver and co-workers (Weaver and Lobkis, 2001; Lobkis and Weaver, 2001;
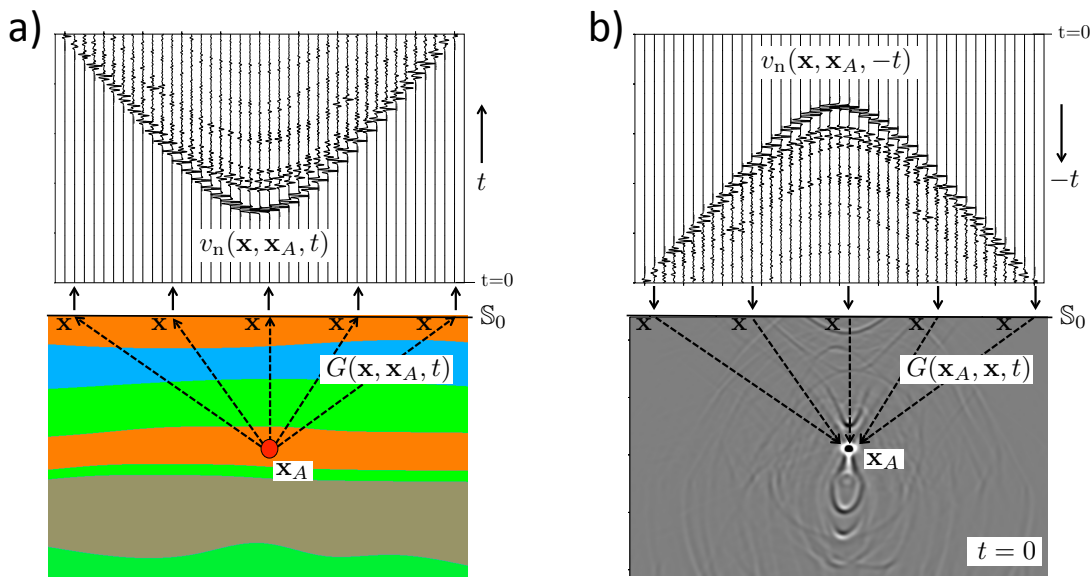
Figure 3. Time-reversal acoustics in a layered medium. (a) Forward propagation from $\mathbf{x}_A$ to the surface $\mathbb{S}_0$. (b) Emission of the time-reversed recordings from $\mathbb{S}_0$ into the medium and snapshot of the wave field at $t = 0$, with focus at $\mathbf{x}_A$.

Weaver and Lobkis, 2002). At ultrasonic scale the object of investigation is often a closed system. Early applications for open systems, including seismological applications, are discussed by Aki (1957), Claerbout (1968), Duvall et al. (1993), Rickett and Claerbout (1999), Schuster (2001), Wapenaar et al. (2002), Campillo and Paul (2003), Derode et al. (2003), Snieder (2004), Schuster et al. (2004), Roux et al. (2005), Sabra et al. (2005a), Larose et al. (2006) and Draganov et al. (2007). A detailed discussion of the many aspects of seismic interferometry is beyond the scope of this paper. Overviews are given by Schuster (2009), Wapenaar et al. (2010) and Nakata et al. (2019).

Figure 4 illustrates the principle. In Figure 4a, a distribution of uncorrelated noise sources $N(\mathbf{x}, t)$ at some boundary $\mathbb{S}_0$ emit waves through an inhomogeneous medium to receivers at $\mathbf{x}_A$ and $\mathbf{x}_B$. The cross-correlation of the responses at $\mathbf{x}_A$ and $\mathbf{x}_B$ converges to $G(\mathbf{x}_B, \mathbf{x}_A, t) * C_N(t)$, where $C_N(t)$ is the autocorrelation of the noise. The result is shown in Figure 4b, for a fixed virtual source at $\mathbf{x}_A$ and an array of receivers at variable $\mathbf{x}_B$.

We use the homogeneous Green's function representation of equation (7) to explain this in a more quantitative way (Wapenaar et al., 2002; Weaver and Lobkis, 2004; van Manen et al., 2005; Korneev and Bakulin, 2006). Representations for elastodynamic interferometry are discussed by Wapenaar (2004), Halliday and Curtis (2008) and Kimman and Trampert (2010). Using a far field approximation for the derivative of the Green's function under the integral in equation (7), we obtain

$$n_i \partial_i G(\mathbf{x}, \mathbf{x}_A, \omega) \rightarrow \frac{i\omega}{c_0} G(\mathbf{x}, \mathbf{x}_A, \omega), \tag{12}$$

where c_0 is the propagation velocity of the homogeneous medium outside $\mathbb{S}$. Substituting this into equation (7) yields

$$G_{\mathrm{h}}(\mathbf{x}_B, \mathbf{x}_A, \omega) \approx \frac{2}{\rho_0 c_0} \oint_{\mathbb{S}} G(\mathbf{x}_B, \mathbf{x}, \omega) G^*(\mathbf{x}_A, \mathbf{x}, \omega) \mathrm{d}\mathbf{x}, \tag{13}$$
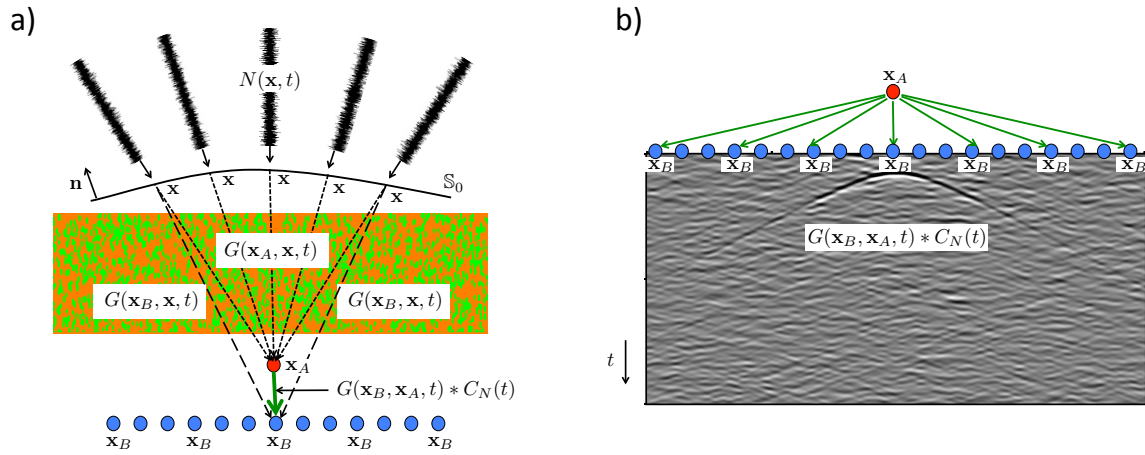
7

Figure 4. Principle of seismic interferometry (artist impression, figures not to scale). (a) Propagation of ambient noise from $\mathbb{S}_0$ through an inhomogeneous medium to receivers at $\mathbf{x}_A$ and $\mathbf{x}_B$. (b) Cross-correlation of responses at $\mathbf{x}_A$ and $\mathbf{x}_B$ (with $\mathbf{x}_A$ fixed and $\mathbf{x}_B$ variable).

or, in the time domain (using equation 2),

$$G(\mathbf{x}_B,\mathbf{x}_A,t) + G(\mathbf{x}_B,\mathbf{x}_A,-t) \approx \frac{2}{\rho_0 c_0} \oint_{\mathbb{S}} G(\mathbf{x}_B,\mathbf{x},t) * G(\mathbf{x}_A,\mathbf{x},-t)\mathrm{d}\mathbf{x}, \tag{14}$$

where ρ_0 is the mass density of the homogeneous medium outside $\mathbb{S}$ (the approximation sign refers to the far-field approximation). For a distribution of noise sources $N(\mathbf{x},t)$ on $\mathbb{S}$ (like in Figure 4a), we can write for the observed field at $\mathbf{x}_A$ and

5   $\mathbf{x}_B$

$$p(\mathbf{x}_A,t) = \oint_{\mathbb{S}} G(\mathbf{x}_A,\mathbf{x},t) * N(\mathbf{x},t)\mathrm{d}\mathbf{x}, \tag{15}$$

$$p(\mathbf{x}_B,t) = \oint_{\mathbb{S}} G(\mathbf{x}_B,\mathbf{x}',t) * N(\mathbf{x}',t)\mathrm{d}\mathbf{x}'. \tag{16}$$

Assuming the noise sources are mutually uncorrelated, they obey

$$\langle N(\mathbf{x}',t) * N(\mathbf{x},-t) \rangle = \delta_{\mathbb{S}}(\mathbf{x} - \mathbf{x}')C_N(t), \tag{17}$$

10   where $C_N(t)$ is the autocorrelation of the noise (which is assumed to be the same for all sources), $\langle \cdot \rangle$ stands for time averaging, and $\delta_{\mathbb{S}}(\mathbf{x} - \mathbf{x}')$ is a 2D delta function defined in $\mathbb{S}$. Cross-correlation of the observed noise fields in $\mathbf{x}_A$ and $\mathbf{x}_B$ gives

$$\langle p(\mathbf{x}_B,t) * p(\mathbf{x}_A,-t) \rangle = \left\langle \oint_{\mathbb{S}} \oint_{\mathbb{S}} G(\mathbf{x}_B,\mathbf{x}',t) * N(\mathbf{x}',t) * G(\mathbf{x}_A,\mathbf{x},-t) * N(\mathbf{x},-t)\mathrm{d}\mathbf{x}'\mathrm{d}\mathbf{x} \right\rangle. \tag{18}$$

Using equation (17) this becomes

$$\langle p(\mathbf{x}_B,t) * p(\mathbf{x}_A,-t) \rangle = \oint_{\mathbb{S}} G(\mathbf{x}_B,\mathbf{x},t) * G(\mathbf{x}_A,\mathbf{x},-t) * C_N(t)\mathrm{d}\mathbf{x}. \tag{19}$$

Note that the right-hand side resembles that of equation (14). Hence, if we convolve both sides of equation (14) with $C_N(t)$, we can replace its right-hand side by the left-hand side of equation (19), according to

$$\{G(\mathbf{x}_B, \mathbf{x}_A, t) + G(\mathbf{x}_B, \mathbf{x}_A, -t)\} * C_N(t) \approx \frac{2}{\rho_0 c_0} \langle p(\mathbf{x}_B, t) * p(\mathbf{x}_A, -t) \rangle. \tag{20}$$

This is the fundamental expression for ambient-noise interferometry. The right-hand side stands for the cross-correlation of the

5 responses at $\mathbf{x}_A$ and $\mathbf{x}_B$. The left-hand side consists of a superposition of the virtual-source response $G(\mathbf{x}_B, \mathbf{x}_A, t) * C_N(t)$ and its time-reversal $G(\mathbf{x}_B, \mathbf{x}_A, -t) * C_N(t)$. It should be noted that, according to equations (15) and (16), it is assumed that the fields $p(\mathbf{x}_A, t)$ and $p(\mathbf{x}_B, t)$ are the responses to noise sources on a closed boundary $\mathbb{S}$. However, in the example in Figure 4, the noise field is emitted into the medium from a finite open boundary $\mathbb{S}_0$. A consequence of this discrepancy is that the retrieved response in Figure 4b lacks the acausal term $G(\mathbf{x}_B, \mathbf{x}_A, -t) * C_N(t)$. Moreover, the causal term $G(\mathbf{x}_B, \mathbf{x}_A, t) * C_N(t)$

10 is blurred by scattering noise, which does not vanish by longer time-averaging. According to equations (15), (16) and (20), the retrieved response would contain the causal and acausal terms and the scattering noise would vanish when the noise field would be emitted from a closed boundary for long enough time.

Figure 4 is exemplary for seismic surface-wave interferometry (Campillo and Paul, 2003; Sabra et al., 2005b; Shapiro and Campillo, 2004; Bensen et al., 2007), in which case Figure 4a should be interpreted as a plan view, with the noise signals

15 representing microseisms, $\mathbb{S}_0$ representing a coast line and the Green's functions representing the fundamental mode of surface waves. The retrieved surface-wave Green's functions are typically used for tomographic imaging (Sabra et al., 2005a; Shapiro et al., 2005; Bensen et al., 2008; Lin et al., 2009). Seismic interferometry can also be used for reflection imaging of the earth's crust with body waves. Because the scattering mechanism is very different, we discuss a second example to illustrate seismic interferometry with body waves. Figure 5a shows the same layered medium as Figure 3a, this time with noise sources at $\mathbb{S}_0$ in

20 the subsurface and the upper surface being a free surface. For this situation the part of the closed-boundary integral over the free surface in equation (6) vanishes. Hence, the closed boundary integrals in equations (15) and (16) can be replaced by open boundary integrals, over the noise sources in the subsurface in Figure 5a. For $p(\mathbf{x}_A, t)$ we take the central trace of Figure 5a (indicated by the red box) and for $p(\mathbf{x}_B, t)$ (with variable $\mathbf{x}_B$) all other traces of this figure. We apply equation (20) to obtain the virtual-source response $G(\mathbf{x}_B, \mathbf{x}_A, t) * C_N(t)$ and its time-reversal $G(\mathbf{x}_B, \mathbf{x}_A, -t) * C_N(t)$, for a fixed virtual source at $\mathbf{x}_A$

25 and receivers at variable $\mathbf{x}_B$. The causal term is shown in Figure 5b. Conform the theory, this is the full reflection response of the layered medium, including multiple reflections. Reflection responses retrieved by body-wave interferometry are typically used for reflection imaging (Kumar and Bostock, 2006; Draganov et al., 2009; Tonegawa et al., 2009; Ruigrok et al., 2012; Oren and Nowack, 2017).

For both methods discussed here (surface-wave interferometry and body-wave interferometry) we assumed that the noise

30 sources are regularly distributed along a part of $\mathbb{S}$ and that they all have the same autocorrelation function. In many practical situations the source distribution is irregular, and the autocorrelations are different for different sources. Several approaches have been developed to account for these issues, such as iterative correlation (Stehly et al., 2008), multidimensional deconvolution (Wapenaar and van der Neut, 2010; van der Neut et al., 2011), directional balancing (Curtis and Halliday, 2010a) and generalized interferometry, circumventing Green's function retrieval (Fichtner et al., 2017).
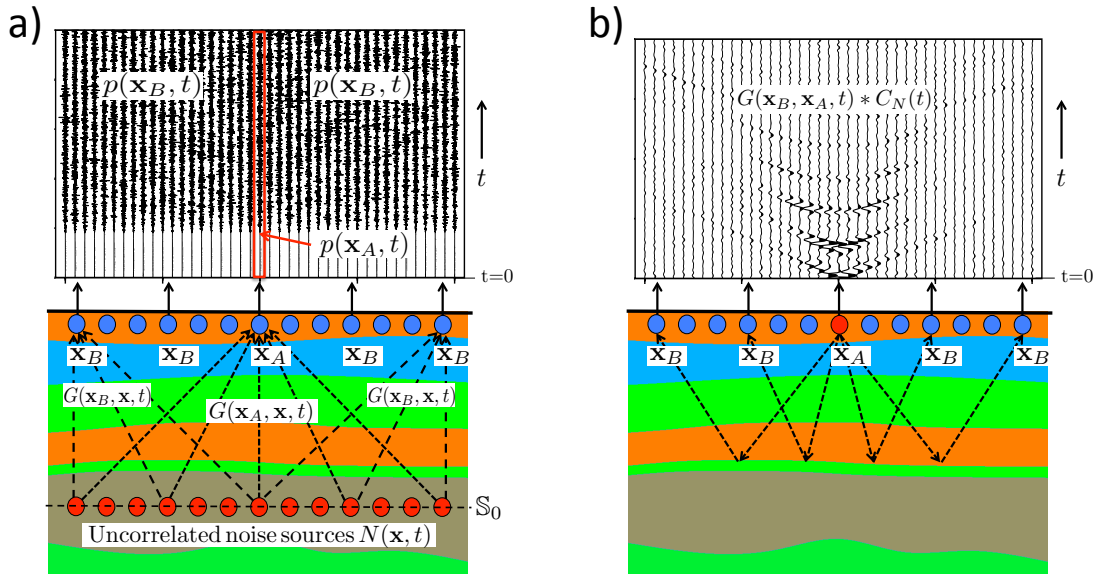
Figure 5. Seismic interferometry with body waves in a layered medium. The upper boundary is a free surface. (a) Noise observed by receivers just below the surface, due to uncorrelated noise sources in the subsurface (only the first 5 seconds of approximately 5 minutes of noise registrations are shown). (b) Retrieved reflection response, including multiple reflections.

2.4 Back propagation

Given a wave field observed at the boundary of a medium, the field inside the medium can be obtained by back propagation (Schneider, 1978; Berkhout, 1982; Fischer and Langenberg, 1984; Wiggins, 1984; Langenberg et al., 1986). Because back propagation implies retrieving a 3D field inside a volume from a 2D field at a boundary, it is also known as holography (Porter and Devaney, 1982; Lindsey and Braun, 2004). Figure 6 illustrates the principle. In Figure 6a, the field at the boundary $\mathbb{S}_0$ due to a source at $\mathbf{x}_A$ inside a layered medium (the same medium as in Figures 3 and 5) is back propagated to an arbitrary point $\mathbf{x}_B$ inside the medium by the time-reversed direct arrival of the Green's function, $G_{\mathrm{d}}(\mathbf{x}, \mathbf{x}_B, -t)$. Figure 6b shows $G_{\mathrm{d}}(\mathbf{x}, \mathbf{x}_B, -t)$ (for fixed $\mathbf{x}_B$) and a snapshot of the back propagated field at time instant $t_1 > 0$ for all $\mathbf{x}_B$. Note that above the source (which is located at $\mathbf{x}_A$) the primary upgoing field coming from the source is clearly retrieved. However, the field below the source is not retrieved. Moreover, several artefacts are present because multiple reflections between the layer interfaces are not accounted for.

A quantitative discussion of back propagation follows from equation (7). By interchanging $\mathbf{x}_A$ and $\mathbf{x}_B$ and multiplying both sides with the spectrum $s(\omega)$ of the source at $\mathbf{x}_A$, we obtain

$$G_{\mathrm{h}}(\mathbf{x}_B, \mathbf{x}_A, \omega)s(\omega) = -2 \oint_{\mathbb{S}} \frac{1}{i\omega\rho(\mathbf{x})} \{\partial_i G^*(\mathbf{x}, \mathbf{x}_B, \omega)\} G(\mathbf{x}, \mathbf{x}_A, \omega)s(\omega)n_i \mathrm{d}\mathbf{x}. \tag{21}$$
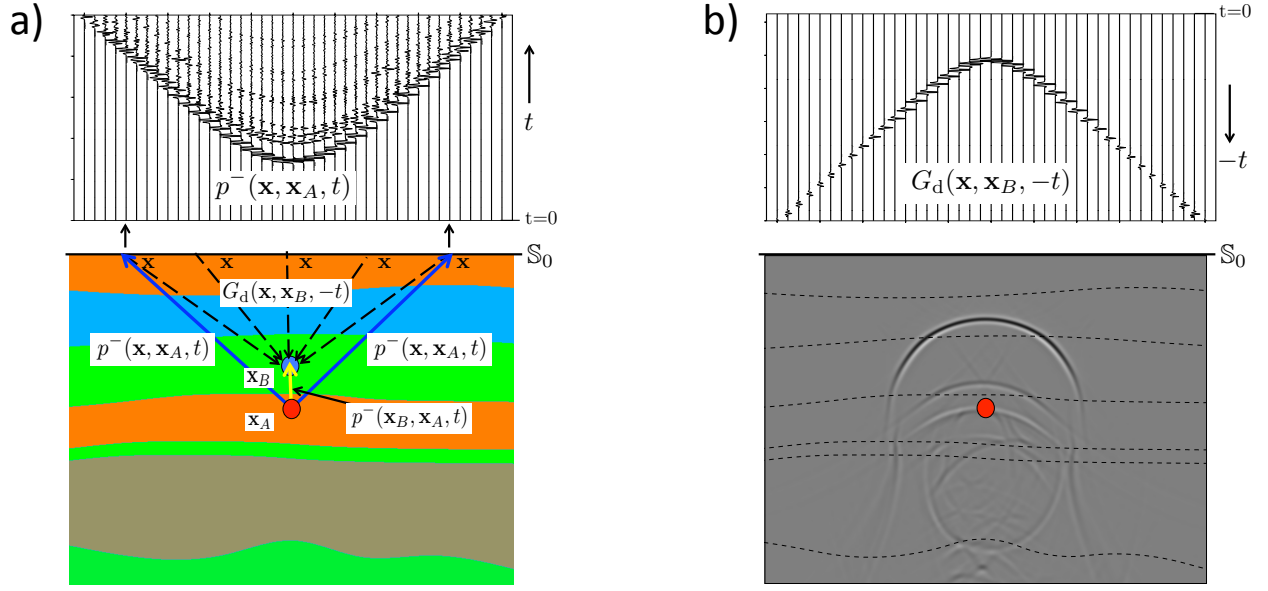
10

Figure 6. Principle of back propagation. (a) The upgoing wave field $p^-(\mathbf{x}, \mathbf{x}_A, t)$ at the boundary $\mathbb{S}_0$ and illustration of its back propagation to $\mathbf{x}_B$ inside the medium. (b) The back propagation operator $G_\mathrm{d}(\mathbf{x}, \mathbf{x}_B, -t)$ (for variable $\mathbf{x}$ along $\mathbb{S}_0$ and fixed $\mathbf{x}_B$) and a snapshot of the back propagated wave field $p^-(\mathbf{x}_B, \mathbf{x}_A, t)$ at $t_1 = 300$ ms for all $\mathbf{x}_B$.

Here $G(\mathbf{x}, \mathbf{x}_A, \omega)s(\omega)$ stands for the observed field $p(\mathbf{x}, \mathbf{x}_A, \omega)$ at the boundary $\mathbb{S}$ and $-\frac{2}{i\omega\rho(\mathbf{x})} n_i \partial_i G^*(\mathbf{x}, \mathbf{x}_B, \omega)$ for the back propagation operator, both in the frequency domain. Hence, in theory the exact field $G_\mathrm{h}(\mathbf{x}_B, \mathbf{x}_A, \omega)s(\omega)$ can be obtained at any $\mathbf{x}_B$ inside the medium. Because in practical situations the field $p(\mathbf{x}, \mathbf{x}_A, \omega)$ is observed only at a finite horizontal part $\mathbb{S}_0$ of the boundary, approximations arise in practise when $\mathbb{S}$ is replaced by $\mathbb{S}_0$. One of the consequences is that multiple reflections
5 are not handled correctly. A detailed analysis (Wapenaar et al., 1989) shows that the primary arrival of the upgoing wave field $p^-(\mathbf{x}_B, \mathbf{x}_A, \omega) = G^-(\mathbf{x}_B, \mathbf{x}_A, \omega)s(\omega)$ is reasonably accurately retrieved with the following approximation of equation (21)

$$p^-(\mathbf{x}_B, \mathbf{x}_A, \omega) \approx \int_{\mathbb{S}_0} F_\mathrm{d}^+(\mathbf{x}, \mathbf{x}_B, \omega) p^-(\mathbf{x}, \mathbf{x}_A, \omega) \mathrm{d}\mathbf{x}. \tag{22}$$

Here the back propagation operator $F_\mathrm{d}^+(\mathbf{x}, \mathbf{x}_B, \omega)$, also known as the focusing operator, is defined as

$$F_\mathrm{d}^+(\mathbf{x}, \mathbf{x}_B, \omega) = \frac{2}{i\omega\rho(\mathbf{x})} \partial_3 G_\mathrm{d}^*(\mathbf{x}, \mathbf{x}_B, \omega), \tag{23}$$

10 where we used $n_3 = -1$ at $\mathbb{S}_0$, considering that the positive x_3-axis is pointing downward. Equations (22) and (23) represent the common approach to back propagation for many applications in seismic imaging and inversion. It works well for primary waves in media with low contrasts but it breaks down when the contrasts are strong and multiple reflections between the layer interfaces cannot be ignored. In section 3.3 we discuss a modified approach to back-propagation which enables the recovery of the full wave field $p(\mathbf{x}_B, \mathbf{x}_A, \omega)$, including the multiple reflections, inside the medium (also below the source at $\mathbf{x}_A$) and which
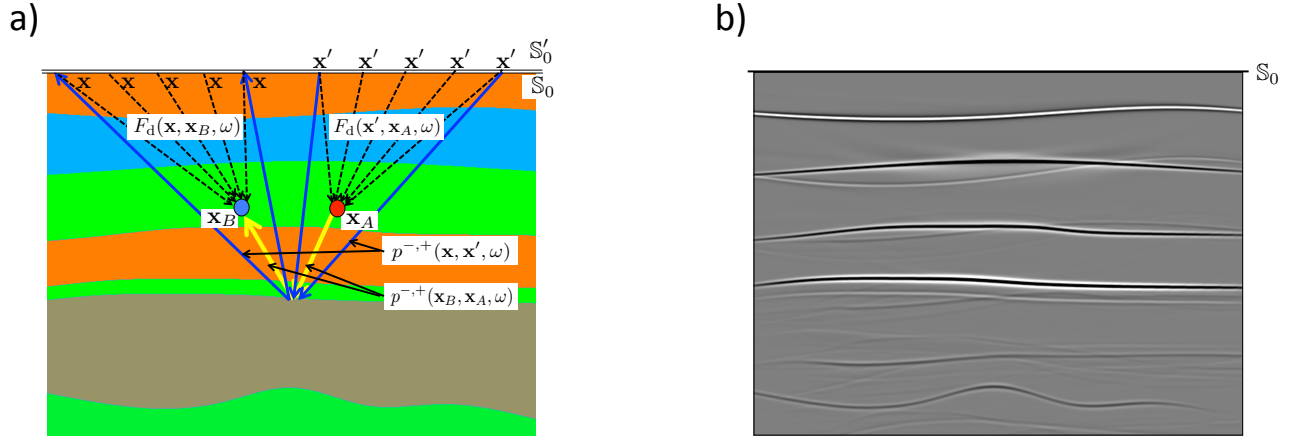15 suppresses artefacts like those in Figure 6b in a data-driven way.

Figure 7. (a) Principle of source-receiver redatuming. (b) Reflectivity image $r(\mathbf{x}_A) \approx p^{-,+}(\mathbf{x}_A, \mathbf{x}_A, t = 0)$ for all $\mathbf{x}_A$.

2.5 Source-receiver redatuming and imaging by double focusing

In the previous section we discussed back propagation of data $p^-(\mathbf{x}, \mathbf{x}_A, \omega)$, which is the response to a source at $\mathbf{x}_A$ inside the medium, observed at $\mathbf{x}$ at the surface. Here we extend this process for the situation in which both the sources and receivers are located at the surface. To this end, we first adapt equations (22) and (23). We replace $\mathbb{S}_0$ by $\mathbb{S}_0'$ (just above $\mathbb{S}_0$), $\mathbf{x}$ by $\mathbf{x}' \in \mathbb{S}_0'$, $\mathbf{x}_A$ by $\mathbf{x} \in \mathbb{S}_0$ and $\mathbf{x}_B$ by $\mathbf{x}_A$, and we add an extra superscript $(+)$ to the wave fields (explained below), which yields

$$p^{-,+}(\mathbf{x}_A, \mathbf{x}, \omega) \approx \int_{\mathbb{S}_0'} F_{\mathrm{d}}^+(\mathbf{x}', \mathbf{x}_A, \omega) p^{-,+}(\mathbf{x}', \mathbf{x}, \omega) \mathrm{d}\mathbf{x}', \tag{24}$$

with

$$F_{\mathrm{d}}^+(\mathbf{x}', \mathbf{x}_A, \omega) = \frac{2}{i\omega\rho(\mathbf{x}')} \partial_3' G_{\mathrm{d}}^*(\mathbf{x}', \mathbf{x}_A, \omega), \tag{25}$$

where ∂_3' stands for differentiation with respect to x_3'. In equation (24), $p^{-,+}(\mathbf{x}', \mathbf{x}, \omega) = G^{-,+}(\mathbf{x}', \mathbf{x}, \omega)s(\omega)$ represents the reflection data at the surface. The first superscript $(-)$ denotes that the field is upgoing at $\mathbf{x}'$; the second superscript $(+)$ denotes that the source at $\mathbf{x}$ emits downgoing waves. Furthermore, $p^{-,+}(\mathbf{x}_A, \mathbf{x}, \omega) = G^{-,+}(\mathbf{x}_A, \mathbf{x}, \omega)s(\omega)$ is the back propagated upgoing field at $\mathbf{x}_A$. Applying source-receiver reciprocity on both sides of equation (24) we obtain

$$p^{-,+}(\mathbf{x}, \mathbf{x}_A, \omega) \approx \int_{\mathbb{S}_0'} p^{-,+}(\mathbf{x}, \mathbf{x}', \omega) F_{\mathrm{d}}^+(\mathbf{x}', \mathbf{x}_A, \omega) \mathrm{d}\mathbf{x}'. \tag{26}$$

The receiver for upgoing waves at $\mathbf{x}_A$ has turned into a source for downgoing waves at $\mathbf{x}_A$, etc. Hence, equation (26) back propagates the sources from $\mathbf{x}'$ on $\mathbb{S}_0'$ to $\mathbf{x}_A$. Substituting this into equation (22), with at both sides p^- replaced by $p^{-,+}$, gives

$$p^{-,+}(\mathbf{x}_B, \mathbf{x}_A, \omega) \approx \int_{\mathbb{S}_0} \int_{\mathbb{S}_0'} F_{\mathrm{d}}^+(\mathbf{x}, \mathbf{x}_B, \omega) p^{-,+}(\mathbf{x}, \mathbf{x}', \omega) F_{\mathrm{d}}^+(\mathbf{x}', \mathbf{x}_A, \omega) \mathrm{d}\mathbf{x}' \mathrm{d}\mathbf{x}. \tag{27}$$

Here $p^{-,+}(\mathbf{x},\mathbf{x}',\omega)$ represents the reflection response at the surface (the blue arrows in Figure 7a). Similarly, $p^{-,+}(\mathbf{x}_B,\mathbf{x}_A,\omega)$ denotes the reflection response to a source for downgoing waves at $\mathbf{x}_A$, observed by a receiver for upgoing waves at $\mathbf{x}_B$ (the yellow arrows in Figure 7a). It is obtained by back propagating sources from $\mathbf{x}'$ to $\mathbf{x}_A$ and receivers from $\mathbf{x}$ to $\mathbf{x}_B$, indicated by the dashed arrows in Figure 7a. In exploration seismology this process is called (source-receiver) redatuming (Berkhout, 1982; Berryhill, 1984) and it is closely related to source-receiver interferometry (Curtis and Halliday, 2010b). For the elastodynamic extension, see Kuo and Dai (1984), Wapenaar and Berkhout (1989) and Hokstad (2000).

The redatumed response $p^{-,+}(\mathbf{x}_B,\mathbf{x}_A,\omega)$ can be used for reflectivity imaging by setting $\mathbf{x}_B$ equal to $\mathbf{x}_A$ and selecting the $t = 0$ component in the time domain, as follows

$$r(\mathbf{x}_A) \approx p^{-,+}(\mathbf{x}_A,\mathbf{x}_A,t=0) = \frac{1}{2\pi}\int\limits_{-\infty}^{\infty} p^{-,+}(\mathbf{x}_A,\mathbf{x}_A,\omega)\mathrm{d}\omega. \tag{28}$$

The combined process (equations 27 and 28) comprises imaging by double focusing (Berkhout, 1982; Wiggins, 1984; Bleistein, 1987; Berkhout and Wapenaar, 1993; Blondel et al., 2018), because it involves twice the application of the focusing operator $F_{\mathrm{d}}^{+}(\mathbf{x},\mathbf{x}_A,\omega)$. By taking the focal point $\mathbf{x}_A$ variable, a reflectivity image of the entire region of interest is obtained. Figure 7b shows the image obtained in this way of the same layered medium as considered in previous examples. Note that the interfaces are clearly imaged, but also that significant artefacts are present because multiple reflections are not correctly handled. In sections 3.4 and 3.5 we discuss more rigorous approaches to source-receiver redatuming and imaging by double focusing, which account for multiple reflections in a data-driven way.

3 Theory and applications of modified single-sided wave field representations

The applications of Green's theorem, discussed in the previous section, are all derived from the classical homogeneous Green's function representation. This representation is exact, but it involves an integral over a closed boundary. In many practical situations the medium of interest is accessible from one side only, which implies that the integration can only be carried out over an open boundary. This induces approximations, of which the incomplete treatment of multiple reflections is the most significant one. In the following we discuss a modification of the homogeneous Green's function representation which involves an integral over an open boundary and yet accounts for all multiple reflections. We call this modified representation the single-sided homogeneous Green's function representation. We discuss how it can be used to improve several of the applications discussed in the previous section.

3.1 Single-sided homogeneous Green's function representations

The classical homogeneous Green's function representations (equations (6) and (7)) are entirely formulated in terms of Green's functions and their time reversals. A Green's function is the causal response to a source at a specific position in space, say at $\mathbf{x}_A$. A time-reversed Green's function can be seen as a focusing function which focuses at $\mathbf{x}_A$. However, this only holds when it converges to $\mathbf{x}_A$ equally from all directions, which can be achieved by emitting it into the medium from a closed boundary. For practical situations we need another type of focusing function, which, when emitted into the medium from a
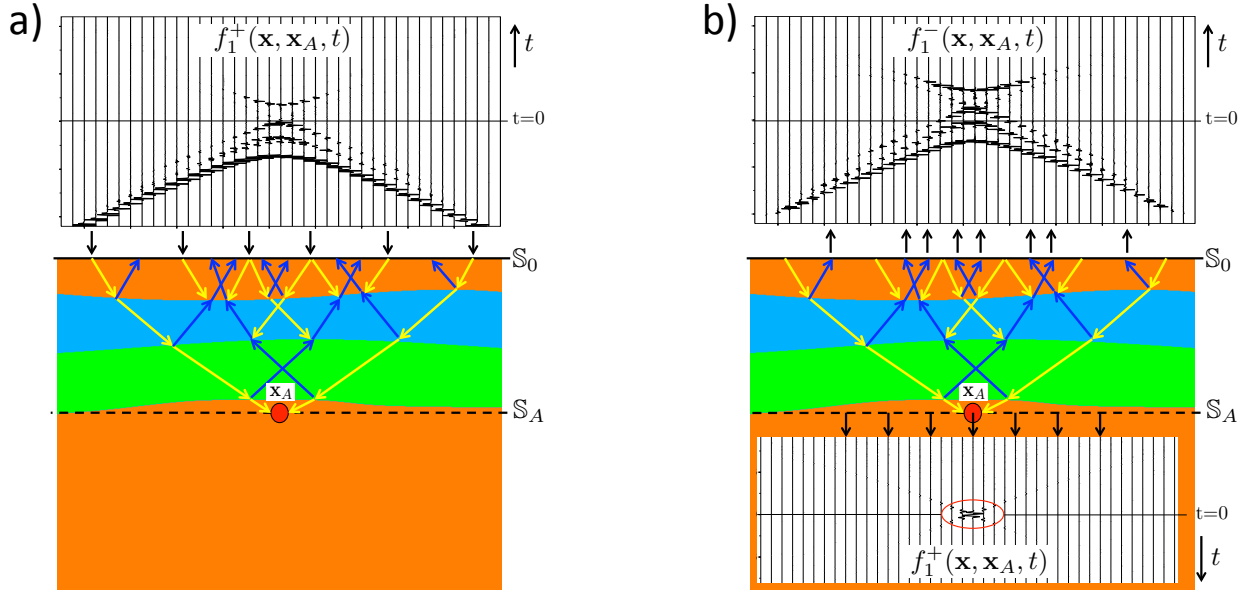
Figure 8. Introduction of the focusing function, to be used in the single-sided homogeneous Green's function representations. (a) Emission of the downgoing part of the focusing function from $\mathbb{S}_0$ into a truncated version of the actual medium. (b) Responses at $\mathbb{S}_0$ and $\mathbb{S}_A$.

single boundary, focuses at $\mathbf{x}_A$. Figure 8 illustrates the principle. It shows a truncated version of the medium, which is identical to the actual medium between the upper boundary $\mathbb{S}_0$ and the focal plane $\mathbb{S}_A$ (the plane which contains the focal point $\mathbf{x}_A$), but it is homogeneous above $\mathbb{S}_0$ and below $\mathbb{S}_A$. In this truncated medium, we define a focusing function $f_1(\mathbf{x}, \mathbf{x}_A, t)$, where $\mathbf{x}_A$ denotes the focal point. At any position $\mathbf{x}$, the focusing function consists of a downgoing and upgoing part, according to

$$f_1(\mathbf{x}, \mathbf{x}_A, t) = f_1^+(\mathbf{x}, \mathbf{x}_A, t) + f_1^-(\mathbf{x}, \mathbf{x}_A, t), \tag{29}$$

where the superscripts $+$ and $-$ indicate downgoing and upgoing, respectively. Figure 8a shows how the downgoing part of the focusing function, $f_1^+(\mathbf{x}, \mathbf{x}_A, t)$, is emitted from $\mathbf{x}$ at $\mathbb{S}_0$ into the medium. The first event (at negative time) propagates downward toward the focal point $\mathbf{x}_A$ (indicated by the outer yellow rays). On its path to the focal point it gets reflected at layer interfaces, indicated by the blue rays. During upward propagation, these blue rays meet new yellow rays (coming from the later events of the focusing function), in such a way that effectively no downward reflection takes place at the layer interfaces, etc. Hence, only the first event of the focusing function reaches the focal depth, where it focuses at $\mathbf{x}_A$. Figure 8b shows the responses to the focusing function, at $\mathbb{S}_0$ and $\mathbb{S}_A$. The response at $\mathbb{S}_0$ is the upgoing part of the focusing function, $f_1^-(\mathbf{x}, \mathbf{x}_A, t)$. The response at $\mathbb{S}_A$ is the downgoing focused field. Because the half-space below $\mathbb{S}_A$ is homogeneous, no upgoing waves reach the focal plane. The focusing conditions at the focal plane are (Wapenaar et al., 2014)

$$[\partial_3 f_1^+(\mathbf{x}, \mathbf{x}_A, t)]_{x_3 = x_{3,A}} = -\tfrac{1}{2}\rho(\mathbf{x}_A)\delta(\mathbf{x}_{\mathrm{H}} - \mathbf{x}_{\mathrm{H},A})\partial_t\delta(t), \tag{30}$$

$$[\partial_3 f_1^-(\mathbf{x}, \mathbf{x}_A, t)]_{x_3 = x_{3,A}} = 0. \tag{31}$$

14

Here $x_{3,A}$ (the x_3-coordinate of the focal point $\mathbf{x}_A$) denotes the depth level of the focal plane $\mathbb{S}_A$; $\mathbf{x}_H = (x_1, x_2)$ and $\mathbf{x}_{H,A} = (x_{1,A}, x_{2,A})$ are horizontal coordinate vectors. Note that the focused field in Figure 8b is a band-limited version of the focus defined in equation (30). This band-limitation is caused by the fact that, for stability reasons, evanescent waves are suppressed in the focusing function.

5   Given the focusing function for a focal point at $\mathbf{x}_A$ and the Green's function for a source at $\mathbf{x}_B$, the single-sided representation of the homogeneous Green's function in the frequency domain reads (Wapenaar et al., 2016a)

$$G_{\mathrm{h}}(\mathbf{x}_B, \mathbf{x}_A, \omega) = 2 \int_{\mathbb{S}_0} \frac{1}{\omega \rho(\mathbf{x})} \Big(\{\partial_i G_{\mathrm{h}}(\mathbf{x}, \mathbf{x}_B, \omega)\} \Im\{f_1(\mathbf{x}, \mathbf{x}_A, \omega)\} - G_{\mathrm{h}}(\mathbf{x}, \mathbf{x}_B, \omega) \Im\{\partial_i f_1(\mathbf{x}, \mathbf{x}_A, \omega)\} \Big) n_i \mathrm{d}\mathbf{x}, \qquad (32)$$

where $\Im$ denotes the imaginary part. The derivation can be found in the supplementary material, section 2.2 (a similar single-sided representation for vectorial wave fields is derived by Wapenaar et al. (2016b) and illustrated with numerical examples by

10   Reinicke Urruticoechea and Wapenaar (2019)). In equation (32), $\mathbb{S}_0$ may be a curved boundary. Moreover, the actual medium, in which the Green's function is defined, may be inhomogeneous above $\mathbb{S}_0$ (in addition to being inhomogeneous below $\mathbb{S}_0$). Note the resemblance with the classical representation of equation (6). Unlike the classical representation, which is exact, equation (32) holds under the assumption that evanescent waves can be neglected. When $\mathbb{S}_0$ is horizontal and the medium above $\mathbb{S}_0$ is homogeneous (for the Green's function as well as for the focusing function), this representation may be approximated by

15   (Van der Neut et al., 2017)

$$G_{\mathrm{h}}(\mathbf{x}_B, \mathbf{x}_A, \omega) = 4 \Re \int_{\mathbb{S}_0} \frac{1}{i \omega \rho(\mathbf{x})} G(\mathbf{x}, \mathbf{x}_B, \omega) \partial_3 \big(f_1^+(\mathbf{x}, \mathbf{x}_A, \omega) - \{f_1^-(\mathbf{x}, \mathbf{x}_A, \omega)\}^* \big) \mathrm{d}\mathbf{x}. \qquad (33)$$

For the derivation, see the supplementary material, section 2.3. For the decomposed Green's function $G^{-,+}(\mathbf{x}_B, \mathbf{x}_A, \omega)$, introduced in section 2.5, we have the following representation (by combining equations 31 and 38 of the supplementary material)

$$G^{-,+}(\mathbf{x}_B, \mathbf{x}_A, \omega) + \chi(\mathbf{x}_B) f_1^-(\mathbf{x}_B, \mathbf{x}_A, \omega) = 2 \int_{\mathbb{S}_0} \frac{1}{i \omega \rho(\mathbf{x})} G^{-,+}(\mathbf{x}, \mathbf{x}_B, \omega) \partial_3 f_1^+(\mathbf{x}, \mathbf{x}_A, \omega) \mathrm{d}\mathbf{x}, \qquad (34)$$

20   where χ is the characteristic function of the medium enclosed by $\mathbb{S}_0$ and $\mathbb{S}_A$. It is defined as

$$\chi(\mathbf{x}_B) = \begin{cases} 1, & \text{for } \mathbf{x}_B \text{ between } \mathbb{S}_0 \text{ and } \mathbb{S}_A, \\ \frac{1}{2}, & \text{for } \mathbf{x}_B \text{ on } \mathbb{S} = \mathbb{S}_0 \cup \mathbb{S}_A, \\ 0, & \text{for } \mathbf{x}_B \text{ outside } \mathbb{S}. \end{cases} \qquad (35)$$

The representations of equations (33) and (34) form the starting point for modifying several of the applications discussed in section 2. These methods, which will be discussed in the subsequent sections, have in common that they make use of focusing functions. The focusing function $f_1^+(\mathbf{x}, \mathbf{x}_A, t)$ for $\mathbf{x}$ at $\mathbb{S}_0$ is by definition the inverse of the transmission response

25   of the truncated medium between $\mathbb{S}_0$ and $\mathbb{S}_A$. Hence, when a detailed model of the medium between these depth levels is available, its transmission response can be numerically modeled and $f_1^+(\mathbf{x}, \mathbf{x}_A, t)$ can be obtained by inverting this transmission response. Next, $f_1^-(\mathbf{x}, \mathbf{x}_A, t)$ can be obtained by applying the reflection response of the truncated medium to $f_1^+(\mathbf{x}, \mathbf{x}_A, t)$. This is obviously a model-driven approach. On the other hand, when the reflection response of the actual medium is available at $\mathbb{S}_0$,

the focusing functions $f_1^+(\mathbf{x},\mathbf{x}_A,t)$ and $f_1^-(\mathbf{x},\mathbf{x}_A,t)$ for $\mathbf{x}$ at $\mathbb{S}_0$ can be retrieved from this reflection response by a 3D extension of the Marchenko method (Wapenaar et al., 2014; Slob et al., 2014). This method needs an initial estimate of $f_1^+(\mathbf{x},\mathbf{x}_A,t)$, for which one should use the inverse of the direct arrival of the transmission response. This requires only a smooth model of the medium between $\mathbb{S}_0$ and $\mathbb{S}_A$. In practice, the back propagating direct arrival of the Green's function, $G_{\mathrm{d}}(\mathbf{x},\mathbf{x}_A,-t)$, is usually

5　taken as initial estimate. Because the 3D Marchenko method uses the reflection response (obtained from measurements) and a smooth model of the medium, it is a data-driven approach for retrieving the focusing functions. A further discussion of the 3D Marchenko method is beyond the scope of this paper.

3.2　Modified time-reversal acoustics

We discuss a modification of time-reversal acoustics. Assuming the focusing functions are available for $\mathbf{x}$ at $\mathbb{S}_0$ (for example

10　from the Marchenko method), we define a new particle velocity field, according to

$$\hat{v}_{\mathrm{n}}^*(\mathbf{x},\mathbf{x}_A,\omega) = \frac{1}{i\omega\rho(\mathbf{x})}\partial_3\big(f_1^+(\mathbf{x},\mathbf{x}_A,\omega) - \{f_1^-(\mathbf{x},\mathbf{x}_A,\omega)\}^*\big)s(\omega), \tag{36}$$

where for $s(\omega)$ we take a real-valued spectrum. Using this in equation (33) we obtain

$$G_{\mathrm{h}}(\mathbf{x}_B,\mathbf{x}_A,\omega)s(\omega) = 4\Re\int_{\mathbb{S}_0} G(\mathbf{x}_B,\mathbf{x},\omega)\hat{v}_{\mathrm{n}}^*(\mathbf{x},\mathbf{x}_A,\omega)\mathrm{d}\mathbf{x}. \tag{37}$$

In the time domain this becomes

15　$$G_{\mathrm{h}}(\mathbf{x}_B,\mathbf{x}_A,t)*s(t) = 2\int_{\mathbb{S}_0} G(\mathbf{x}_B,\mathbf{x},t)*\hat{v}_{\mathrm{n}}(\mathbf{x},\mathbf{x}_A,-t)\mathrm{d}\mathbf{x} + 2\int_{\mathbb{S}_0} G(\mathbf{x}_B,\mathbf{x},-t)*\hat{v}_{\mathrm{n}}(\mathbf{x},\mathbf{x}_A,t)\mathrm{d}\mathbf{x}. \tag{38}$$

The first integral is the same as that in equation (10) (except that $\hat{v}_{\mathrm{n}}$ is defined differently), whereas the second integral is the time reversal of the first one. For ultrasonic applications, assuming there are receivers at one or more $\mathbf{x}_B$ locations, the field $\hat{v}_{\mathrm{n}}(\mathbf{x},\mathbf{x}_A,-t)$ can be emitted physically into the real medium and its response can be measured at $\mathbf{x}_B$. The homogeneous Green's function is then obtained by superposing this response and its time reversal. For geophysical applications, the first

20　integral can, at least in theory, be evaluated by numerically emitting the field $\hat{v}_{\mathrm{n}}(\mathbf{x},\mathbf{x}_A,-t)$ into a model of the earth. The superposition of this integral and its time-reversal gives the homogeneous Green's function. Following either one of these procedures, the result obtained at $t=0$ is shown in Figure 9b. For comparison, Figure 9a once more shows the classical time-reversal result of Figure 3b. Note the different character of the fields v_{n} and $\hat{v}_{\mathrm{n}}$ in the upper panels, which have only one event in common. The snapshots at $t=0$ in the lower panels are also very different: the artefacts in Figure 9a are almost entirely

25　absent in Figure 9b. The latter figure only shows a clear focus at $\mathbf{x}_A$.

Obtaining an accurate focus as in Figure 9b by numerically emitting the field $\hat{v}_{\mathrm{n}}(\mathbf{x},\mathbf{x}_A,-t)$ into the earth requires a very accurate model of the earth, which should include accurate information on the position, structure and contrast of the layer interfaces. This requirement can be overcome by also retrieving the Green's function $G(\mathbf{x}_B,\mathbf{x},t)$ in equation (38) with the Marchenko method and evaluating the integrals for all $\mathbf{x}_B$. This is not further discussed here. Alternative methods that don't

30　need information about the layer interfaces are discussed in sections 3.3 to 3.5 and illustrated with examples.
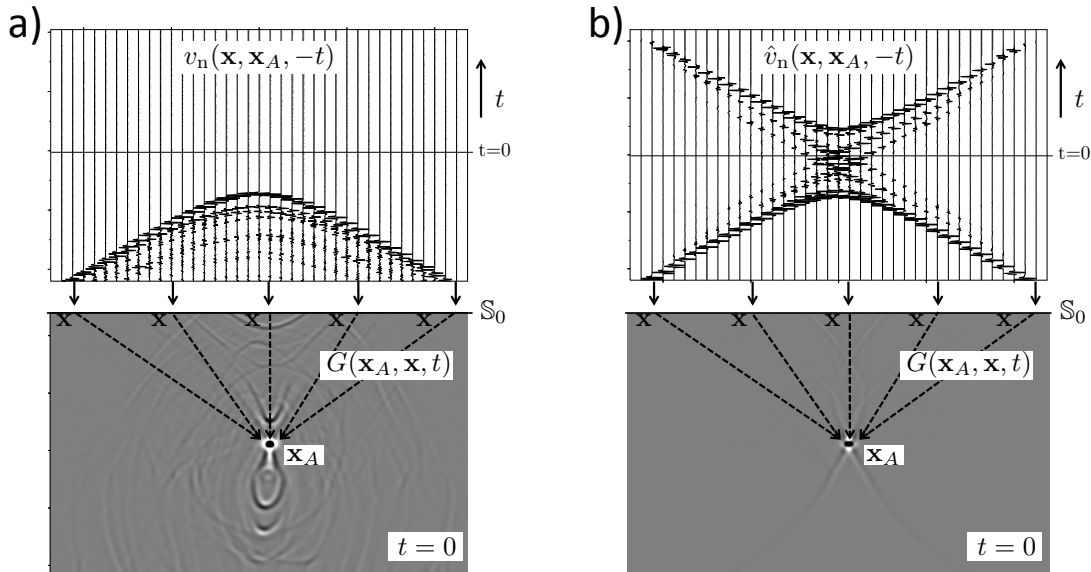
Figure 9. Modified time-reversal acoustics in a layered medium. (a) Classical approach: emission of the time-reversed recordings from $\mathbb{S}_0$ into the medium. (b) Emission of a modified field, defined by equation (36), into the medium. Note the improved focus.

3.3 Modified back propagation

We modify the approach for back propagation. By interchanging $\mathbf{x}_A$ and $\mathbf{x}_B$ in equation (33) and multiplying both sides with a real-valued source spectrum $s(\omega)$, we obtain

$$p(\mathbf{x}_B, \mathbf{x}_A, \omega) + p^*(\mathbf{x}_B, \mathbf{x}_A, \omega) = 2\Re \int_{\mathbb{S}_0} F(\mathbf{x}, \mathbf{x}_B, \omega) p(\mathbf{x}, \mathbf{x}_A, \omega) \mathrm{d}\mathbf{x}, \tag{39}$$

5   with $p(\mathbf{x}, \mathbf{x}_A, \omega) = G(\mathbf{x}, \mathbf{x}_A, \omega) s(\omega)$ and

$$F(\mathbf{x}, \mathbf{x}_B, \omega) = \frac{2}{i\omega\rho(\mathbf{x})} \partial_3 \big(f_1^+(\mathbf{x}, \mathbf{x}_B, \omega) - \{f_1^-(\mathbf{x}, \mathbf{x}_B, \omega)\}^* \big). \tag{40}$$

Note that the operator $F_{\mathrm{d}}^+(\mathbf{x}, \mathbf{x}_B, \omega)$ in equation (23) is an approximation of the operator $F(\mathbf{x}, \mathbf{x}_B, \omega)$ in equation (40). It is obtained by omitting the term $\{f_1^-(\mathbf{x}, \mathbf{x}_B, \omega)\}^*$ and replacing the term $f_1^+(\mathbf{x}, \mathbf{x}_B, \omega)$ by its initial estimate, i.e, the Fourier transform of the direct arrival of the Green's function, $G_{\mathrm{d}}(\mathbf{x}, \mathbf{x}_B, -t)$. Figure 10 illustrates, in the time domain, the principle of

10   modified back propagation. In Figure 10a, the field $p(\mathbf{x}, \mathbf{x}_A, t)$ is back propagated to an arbitrary point $\mathbf{x}_B$ inside the medium by operator $F(\mathbf{x}, \mathbf{x}_B, t)$. This operator can be obtained from reflection data at the surface and the initial estimate $G_{\mathrm{d}}(\mathbf{x}, \mathbf{x}_B, -t)$, using the 3D Marchenko method. Figure 10b shows $F(\mathbf{x}, \mathbf{x}_B, t)$ (for fixed $\mathbf{x}_B$) and a snapshot of the back propagated field at a time instant $t_1 > 0$ for all $\mathbf{x}_B$. Note that the full field $p(\mathbf{x}_B, \mathbf{x}_A, t)$ is retrieved (downgoing and upgoing components, primaries and multiples) and that hardly any artefacts are visible. The dashed lines in the snapshot in Figure 10b indicate the interfaces to aid the interpretation of the snapshot. Note, however, that these interfaces need not be known to obtain this result: only a
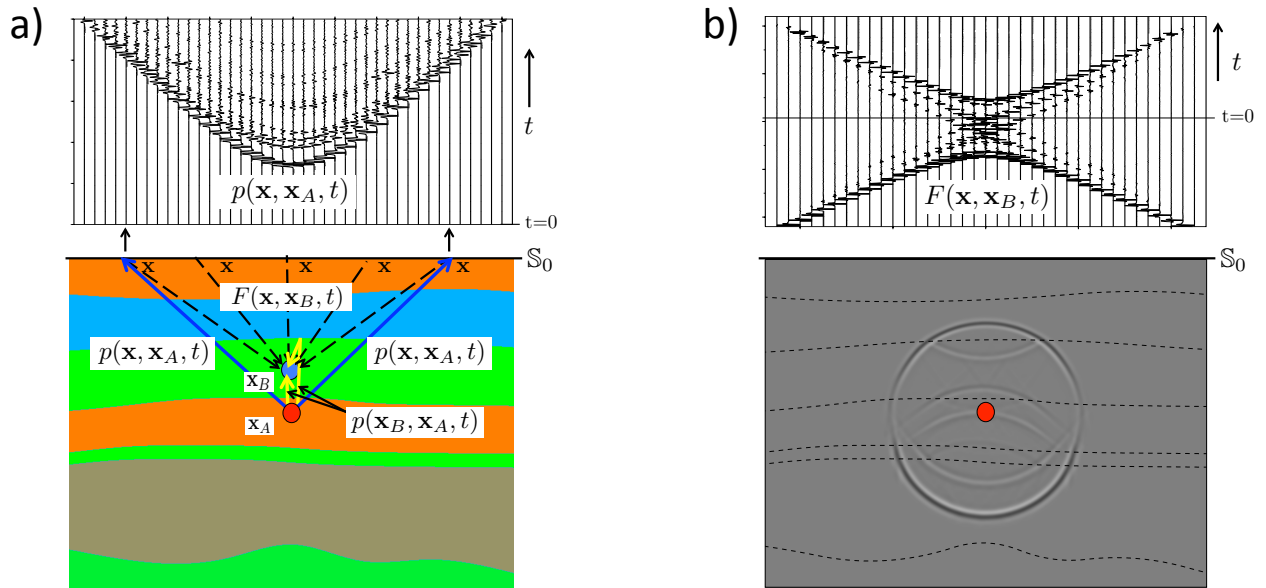
15

17

Figure 10. Principle of modified back propagation. (a) The wave field $p(\mathbf{x}, \mathbf{x}_A, t)$ at the boundary $\mathbb{S}_0$ and illustration of its back propagation to $\mathbf{x}_B$ inside the medium. (b) The back propagation operator $F(\mathbf{x}, \mathbf{x}_B, t)$ (for variable $\mathbf{x}$ along $\mathbb{S}_0$ and fixed $\mathbf{x}_B$) and a snapshot of the back propagated wave field $p(\mathbf{x}_B, \mathbf{x}_A, t)$ at $t_1 = 300$ ms for all $\mathbf{x}_B$.

smooth subsurface model is required to define the initial estimate $G_{\mathrm{d}}(\mathbf{x}, \mathbf{x}_B, -t)$ of the focusing operator. All other events in the focusing operator come directly from the reflection data at the surface.

This back propagation method has an interesting application in monitoring of induced seismicity. Assuming $p(\mathbf{x}, \mathbf{x}_A, t)$ stands for the response to an induced seismic source at $\mathbf{x}_A$, this method creates, in a data-driven way, omnidirectional virtual receivers at any $\mathbf{x}_B$ to monitor the emitted field from the source to the surface. This application is extensively discussed in the companion paper (Brackenhoff et al., 2019).

3.4 Modified source-receiver redatuming

We modify the approach for source-receiver redatuming. First, in equation (39), we replace $\mathbb{S}_0$ by $\mathbb{S}_0'$ (just above $\mathbb{S}_0$), $\mathbf{x}$ by $\mathbf{x}' \in \mathbb{S}_0'$, $\mathbf{x}_A$ by $\mathbf{x} \in \mathbb{S}_0$ and $\mathbf{x}_B$ by $\mathbf{x}_A$. Next, we apply source-receiver reciprocity on both sides of the equation. This yields

$$p(\mathbf{x}, \mathbf{x}_A, \omega) + p^*(\mathbf{x}, \mathbf{x}_A, \omega) = 2\Re \int_{\mathbb{S}_0'} p(\mathbf{x}, \mathbf{x}', \omega) F(\mathbf{x}', \mathbf{x}_A, \omega) \mathrm{d}\mathbf{x}', \tag{41}$$

with $F(\mathbf{x}', \mathbf{x}_A, \omega)$ defined as in equation (40), with ∂_3 replaced by ∂_3', similar as in equation (25). The field $p(\mathbf{x}, \mathbf{x}', \omega) = G(\mathbf{x}, \mathbf{x}', \omega) s(\omega)$ represents the data at the surface. Equation (41) back propagates the sources from $\mathbf{x}'$ on $\mathbb{S}_0'$ to $\mathbf{x}_A$. Source-receiver redatuming is now defined as the following two-step process. In step one, apply equation (41) to create an omnidirectional virtual source at any desired position $\mathbf{x}_A$ in the subsurface. According to the left-hand side, the response to this virtual
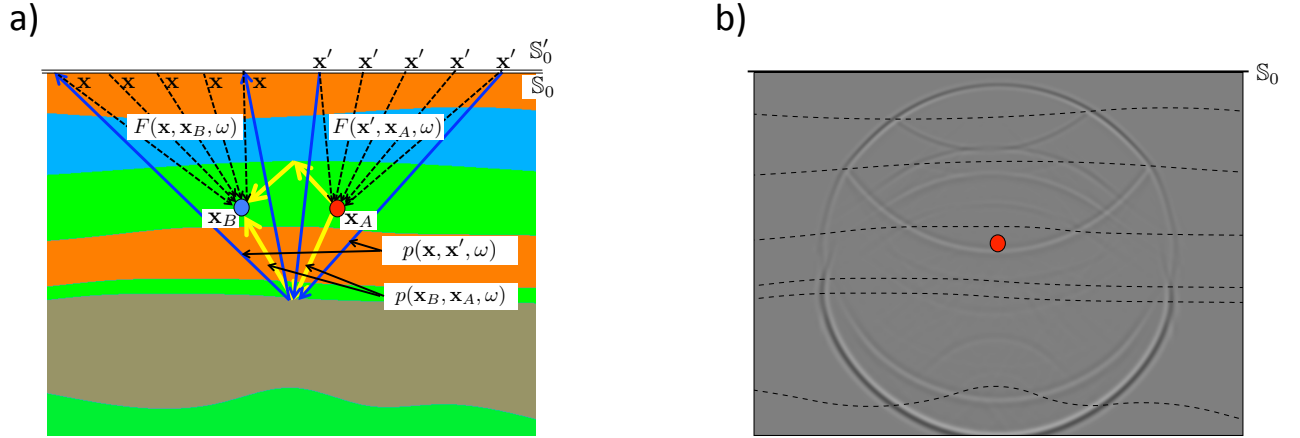
Figure 11. (a) Principle of modified source-receiver redatuming. (b) Snapshot of the wave field $p(\mathbf{x}_B, \mathbf{x}_A, t)$ at $t_2 = 500$ ms for all $\mathbf{x}_B$.

source is observed by actual receivers at $\mathbf{x}$ at the surface. Isolate $p(\mathbf{x}, \mathbf{x}_A, \omega)$ from the left-hand side by applying a time window (a simple Heaviside function) in the time domain. In step two, substitute the retrieved response $p(\mathbf{x}, \mathbf{x}_A, \omega)$ into equation (39) to create virtual receivers at any position $\mathbf{x}_B$ in the subsurface. Figure 11(a) illustrates the principle. The operators can be obtained with the 3D Marchenko method. Figure 11b shows a snapshot of $p(\mathbf{x}_B, \mathbf{x}_A, t)$ at a time instant $t_2 > t_1 > 0$ for all $\mathbf{x}_B$

5   (the retrieved snapshot at t_1 is indistinguishable from that in Figure 10b, which is why we chose to show a snapshot at another time instant). The dashed lines in the snapshot in Figure 11b indicate the interfaces to aid the interpretation of the snapshot, but the interfaces need not to be known to obtain this result. This method has an interesting application in forecasting the effects of induced seismicity. Assuming $\mathbf{x}_A$ is the position where induced seismicity is likely to take place, this method forecasts the response by creating, in a data-driven way, a virtual source at $\mathbf{x}_A$ and virtual receivers at any $\mathbf{x}_B$ that observe the propagation

10 and scattering of its emitted field from the source to the surface. Also this method is extensively discussed in the companion paper (Brackenhoff et al., 2019).

3.5 Modified imaging by double focusing

If we would apply imaging to the retrieved response $p(\mathbf{x}_B, \mathbf{x}_A, \omega) + p^*(\mathbf{x}_B, \mathbf{x}_A, \omega)$ in a similar way as in equation (28), we would obtain an image of the virtual sources instead of the reflectivity. Similar as in section 2.5 we need a process to obtain the

15 decomposed response $p^{-,+}(\mathbf{x}_B, \mathbf{x}_A, \omega)$. Our starting point is equation (34), in which we interchange $\mathbf{x}_A$ and $\mathbf{x}_B$ and choose both at $\mathbb{S}_A$, such that $f_1^-(\mathbf{x}_A, \mathbf{x}_B, \omega) = 0$. Applying source-receiver reciprocity on the left-hand side and multiplying both sides with a source spectrum $s(\omega)$, we obtain

$$p^{-,+}(\mathbf{x}_B, \mathbf{x}_A, \omega) = \int_{\mathbb{S}_0} F^+(\mathbf{x}, \mathbf{x}_B, \omega) p^{-,+}(\mathbf{x}, \mathbf{x}_A, \omega) \mathrm{d}\mathbf{x}, \tag{42}$$
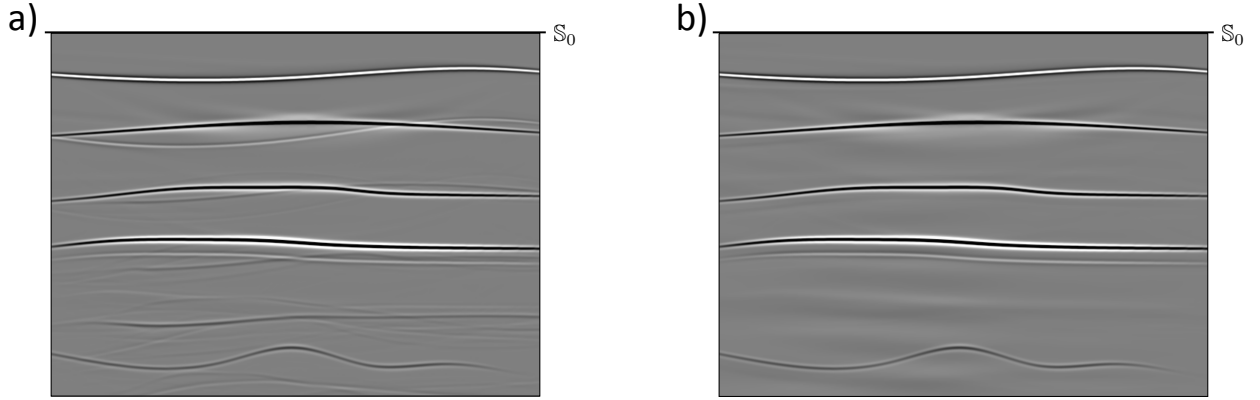
19

Figure 12. Reflectivity images obtained by the double-focusing method. (a) Classical approach. (b) Modified approach.

with $p^{-,+}(\mathbf{x},\mathbf{x}_A,\omega) = G^{-,+}(\mathbf{x},\mathbf{x}_A,\omega)s(\omega)$ and

$$F^+(\mathbf{x},\mathbf{x}_B,\omega) = \frac{2}{i\omega\rho(\mathbf{x})}\partial_3 f_1^+(\mathbf{x},\mathbf{x}_B,\omega). \tag{43}$$

Next, in equation (34), replace $\mathbb{S}_0$ by $\mathbb{S}'_0$ (just above $\mathbb{S}_0$), $\mathbf{x}$ by $\mathbf{x}' \in \mathbb{S}'_0$ and $\mathbf{x}_B$ by $\mathbf{x} \in \mathbb{S}_0$. Applying source-receiver reciprocity on the right-hand side and multiplying both sides with a source spectrum $s(\omega)$, we obtain

$$p^{-,+}(\mathbf{x},\mathbf{x}_A,\omega) = \int_{\mathbb{S}'_0} p^{-,+}(\mathbf{x},\mathbf{x}',\omega)F^+(\mathbf{x}',\mathbf{x}_A,\omega)\mathrm{d}\mathbf{x}' - f_1^-(\mathbf{x},\mathbf{x}_A,\omega)s(\omega), \tag{44}$$

with $F^+(\mathbf{x}',\mathbf{x}_A,\omega)$ defined as in equation (43), with ∂_3 replaced by ∂'_3, similar as in equation (25). Substitution of equation (44) into equation (42) yields

$$p^{-,+}(\mathbf{x}_B,\mathbf{x}_A,\omega) = \int_{\mathbb{S}_0}\int_{\mathbb{S}'_0} F^+(\mathbf{x},\mathbf{x}_B,\omega)p^{-,+}(\mathbf{x},\mathbf{x}',\omega)F^+(\mathbf{x}',\mathbf{x}_A,\omega)\mathrm{d}\mathbf{x}'\mathrm{d}\mathbf{x} \tag{45}$$

$$- \int_{\mathbb{S}_0} F^+(\mathbf{x},\mathbf{x}_B,\omega)f_1^-(\mathbf{x},\mathbf{x}_A,\omega)s(\omega)\mathrm{d}\mathbf{x}.$$

This is the modified version of equation (27), with the operators F_d^+, which account for primaries only, replaced by operators F^+, accounting for primaries and multiples. These operators can be obtained with the 3D Marchenko method from the reflection data $p^{-,+}(\mathbf{x},\mathbf{x}',\omega)$ and a smooth model of the medium to define the initial estimate of f_1^+. The second term on the right-hand side can be removed by a time-window in the time domain, which leaves the redatumed reflection response $p^{-,+}(\mathbf{x}_B,\mathbf{x}_A,\omega)$. The reflectivity imaging step to retrieve $r(\mathbf{x}_A)$ is the same as that in equation (28) and is not repeated here. Figure 12b shows an image obtained by applying equations (45) and (28) for all $\mathbf{x}_A$ in the region of interest, for the same medium that was imaged with the classical double-focusing method (which for ease of comparison is repeated in Figure 12a). Note that the artefacts, caused by the internal multiple reflections, have almost entirely been removed. In practical situations the modified method may suffer from imperfections in the data, such as incomplete sampling, anelastic losses, out-of plane

reflections, 3D spreading effects, etc. Several of these imperfections can be accounted for by making the method adaptive (van der Neut et al., 2014). Promising results have been obtained with real data (Ravasi et al., 2016; Staring et al., 2018).

Other methods exist that deal with internal multiple reflections in imaging. Davydenko and Verschuur (2017) discuss a method called full wavefield migration. This is a recursive method, starting at the surface, which alternately resolves layer interfaces and predicts the multiples related to these interfaces. In contrast, equation (45) is non-recursive. The field $p^{-,+}(\mathbf{x}_B, \mathbf{x}_A, \omega)$ at $\mathbb{S}_A$ is obtained without needing information about the layer interfaces between $\mathbb{S}_0$ and $\mathbb{S}_A$; a smooth model suffices. Weglein et al. (1997, 2011), Jakubowicz (1998) and Ten Kroode (2002) propose methods that eliminate the internal multiples directly from the reflection data at the surface, without needing model information. These methods work well for first order internal multiples, but higher order internal multiples are predicted only with approximate amplitudes. Variants of the Marchenko method have been developed that also aim to eliminate the internal multiples from the reflection data at the surface (Meles et al., 2015; van der Neut and Wapenaar, 2016; Zhang et al., 2019). The last reference shows that all orders of multiples are, at least in theory, predicted with the correct amplitudes without needing model information. Once the internal multiples have been successfully eliminated from the reflection data at the surface, standard redatuming and imaging (for example as described in section 2.5) can be used to form an accurate image of the subsurface, without artefacts caused by multiple reflections.

4 Conclusions

The classical homogeneous Green's function representation, originally developed for optical image formation by holograms, expresses the Green's function plus its time-reversal between two arbitrary points in terms of an integral along a closed boundary enclosing these points. It forms a unified basis for a variety of seismic imaging methods, such as time-reversal acoustics, seismic interferometry, back propagation, source-receiver redatuming and imaging by double focusing. We have derived each of these methods by applying some simple manipulations to the classical homogeneous Green's function representation, which implies that these methods are all different sides of the same coin. As a consequence, they share the same advantages and limitations. Because the underlying representation is exact, it accounts for all orders of multiple scattering. This property is, to some extent, exploited by time-reversal acoustics in a medium with random scatterers and by seismic interferometry in a layered medium below a free surface. However, in most cases multiple scattering is not correctly handled because in practical situations data are not available on a closed boundary. We also discussed a single-sided homogeneous Green's function representation, which requires access to the medium from one side only, say from the earth's surface. This single-sided representation ignores evanescent waves, but it accounts for all orders of multiple scattering, similar as the classical closed-boundary representation. We used the single-sided representation as the basis for deriving modifications of time-reversal acoustics, back propagation, source-receiver redatuming and imaging by double focusing. These methods do account for multiple scattering and can be used to obtain accurate images of the source or the subsurface, without artefacts related to multiple scattering. Another interesting application is the monitoring and forecasting of responses to induced seismic sources, which is discussed in detail in a companion paper.

Code availability. The modeling and imaging software that has been used to generate the numerical examples in this paper can be downloaded from https://github.com/JanThorbecke/OpenSource

Author contributions. JB and JT developed software and generated the numerical examples. KW wrote the paper. All authors reviewed the manuscript.

5   *Competing interests.* The authors declare that they have no competing interests.

References

Aki, K.: Space and time spectra of stationary stochastic waves, with special reference to micro-tremors, Bulletin of the Earthquake Research Institute, 35, 415–457, 1957.

Anderson, B. E., Guyer, R. A., Ulrich, T. J., Le Bas, P.-Y., Larmat, C., Griffa, M., and Johnson, P. A.: Energy current imaging method for time reversal in elastic media, Applied Physics Letters, 95, 021 907, 2009.

Baysal, E., Kosloff, D. D., and Sherwood, J. W. C.: Reverse time migration, Geophysics, 48, 1514–1524, 1983.

Bensen, G. D., Ritzwoller, M. H., Barmin, M. P., Levshin, A. L., Lin, F., Moschetti, M. P., Shapiro, N. M., and Yang, Y.: Processing seismic ambient noise data to obtain reliable broad-band surface wave dispersion measurements, Geophysical Journal International, 169, 1239–1260, 2007.

Bensen, G. D., Ritzwoller, M. H., and Shapiro, N. M.: Broadband ambient noise surface wave tomography across the United States, Journal of Geophysical Research - Solid Earth, 113, B05 306, 2008.

Berkhout, A. J.: Seismic Migration. Imaging of acoustic energy by wave field extrapolation. A. Theoretical aspects, Elsevier, 1982.

Berkhout, A. J. and Wapenaar, C. P. A.: A unified approach to acoustical reflection imaging. Part II: The inverse problem, Journal of the Acoustical Society of America, 93, 2017–2023, 1993.

Berryhill, J. R.: Wave-equation datuming before stack, Geophysics, 49, 2064–2066, 1984.

Bleistein, N.: On the imaging of reflectors in the Earth, Geophysics, 52, 931–942, 1987.

Blondel, T., Chaput, J., Derode, A., Campillo, M., and Aubry, A.: Matrix approach of seismic imaging: Application on the Erebus Volcano, Antarctica, Journal of Geophysical Research, 114, (early view), 2018.

Bozdağ, E., Peter, D., Lefebvre, M., Komatitsch, D., Tromp, J., Hill, J., Podhorszki, N., and Pugmire, D.: Global adjoint tomography: first-generation model, Geophysical Journal International, 207, 1739–1766, 2016.

Brackenhoff, J., Thorbecke, J., and Wapenaar, K.: Monitoring induced distributed double-couple sources using Marchenko-based virtual receivers, Solid Earth, 10, (this issue), 2019.

Campillo, M. and Paul, A.: Long-range correlations in the diffuse seismic coda, Science, 299, 547–549, 2003.

Cassereau, D. and Fink, M.: Time-reversal of ultrasonic fields - Part III: Theory of the closed time-reversal cavity, IEEE Transactions on Ultrasonics, Ferroelectrics, and Frequency Control, 39, 579–592, 1992.

Challis, L. and Sheard, F.: The Green of Green functions, Physics Today, 56, 41–46, 2003.

Claerbout, J. F.: Synthesis of a layered medium from its acoustic transmission response, Geophysics, 33, 264–269, 1968.

Clapp, R. G., Fu, H., and Lindtjorn, O.: Selecting the right hardware for reverse time migration, The Leading Edge, 29, 48–58, 2010.

Curtis, A. and Halliday, D.: Directional balancing for seismic and general wavefield interferometry, Geophysics, 75, SA1–SA14, 2010a.

Curtis, A. and Halliday, D.: Source-receiver wavefield interferometry, Physical Review E, 81, 046 601, 2010b.

Davydenko, M. and Verschuur, D. J.: Full-wavefield migration: using surface and internal multiples in imaging, Geophysical Prospecting, 65, 7–21, 2017.

Derode, A., Roux, P., and Fink, M.: Robust acoustic time reversal with high-order multiple scattering, Physical Review Letters, 75, 4206–4209, 1995.

Derode, A., Larose, E., Tanter, M., de Rosny, J., Tourin, A., Campillo, M., and Fink, M.: Recovering the Green's function from field-field correlations in an open scattering medium (L), Journal of the Acoustical Society of America, 113, 2973–2976, 2003.

Douma, J. and Snieder, R.: Focusing of elastic waves for microseismic imaging, Geophysical Journal International, 200, 390–401, 2015.

Draeger, C. and Fink, M.: One-channel time-reversal in chaotic cavities: Theoretical limits, Journal of the Acoustical Society of America, 105, 611–617, 1999.

Draganov, D., Wapenaar, K., Mulder, W., Singer, J., and Verdel, A.: Retrieval of reflections from seismic background-noise measurements, Geophysical Research Letters, 34, L04 305, 2007.

5   Draganov, D., Campman, X., Thorbecke, J., Verdel, A., and Wapenaar, K.: Reflection images from ambient seismic noise, Geophysics, 74, A63–A67, 2009.

Duvall, T. L., Jefferies, S. M., Harvey, J. W., and Pomerantz, M. A.: Time-distance helioseismology, Nature, 362, 430–432, 1993.

Esmersoy, C. and Oristaglio, M.: Reverse-time wave-field extrapolation, imaging, and inversion, Geophysics, 53, 920–931, 1988.

Etgen, J., Gray, S. H., and Zhang, Y.: An overview of depth imaging in exploration geophysics, Geophysics, 74, WCA5–WCA17, 2009.

10   Fichtner, A., Stehly, L., Ermert, L., and Boehm, C.: Generalized interferometry − I: theory for interstation correlations, Geophysical Journal International, 208, 603–638, 2017.

Fink, M.: Time-reversal of ultrasonic fields: Basic principles, IEEE Transactions on Ultrasonics, Ferroelectrics, and Frequency Control, 39, 555–566, 1992.

Fink, M.: Time-reversal acoustics in complex environments, Geophysics, 71, SI151–SI164, 2006.

15   Fischer, M. and Langenberg, K. J.: Limitations and defects of certain inverse scattering theories, IEEE Trans. Ant. Prop., 32, 1080–1088, 1984.

Gajewski, D. and Tessmer, E.: Reverse modelling for seismic event characterization, Geophysical Journal International, 163, 276–284, 2005.

Green, G.: An essay on the application of mathematical analysis to the theories of electricity and magnetism, Privately published, 1828.

Halliday, D. and Curtis, A.: Seismic interferometry, surface waves and source distribution, Geophysical Journal International, 175, 1067–

20   1087, 2008.

Hokstad, K.: Multicomponent Kirchhoff migration, Geophysics, 65, 861–873, 2000.

Jakubowicz, H.: Wave equation prediction and removal of interbed multiples, in: SEG, Expanded Abstracts, pp. 1527–1530, 1998.

Kimman, W. P. and Trampert, J.: Approximations in seismic interferometry and their effects on surface waves, Geophysical Journal International, 182, 461–476, 2010.

25   Korneev, V. and Bakulin, A.: On the fundamentals of the virtual source method, Geophysics, 71, A13–A17, 2006.

Kumar, M. R. and Bostock, M. G.: Transmission to reflection transformation of teleseismic wavefields, Journal of Geophysical Research - Solid Earth, 111, B08 306, 2006.

Kuo, J. T. and Dai, T. F.: Kirchhoff elastic wave migration for the case of noncoincident source and receiver, Geophysics, 49, 1223–1238, 1984.

Langenberg, K. J., Berger, M., Kreutter, T., Mayer, K., and Schmitz, V.: Synthetic aperture focusing technique signal processing, NDT International, 19, 177–189, 1986.

Larmat, C., Guyer, R. A., and Johnson, P. A.: Time-reversal methods in geophysics, Physics Today, 63, 31–35, 2010.

Larose, E., Margerin, L., Derode, A., van Tiggelen, B., Campillo, M., Shapiro, N., Paul, A., Stehly, L., and Tanter, M.: Correlation of random wave fields: An interdisciplinary review, Geophysics, 71, SI11–SI21, 2006.

35   Lin, F.-C., Ritzwoller, M. H., and Snieder, R.: Eikonal tomography: surface wave tomography by phase front tracking across a regional broad-band seismic array, Geophysical Journal International, 177, 1091–1110, 2009.

Lindsey, C. and Braun, D. C.: Principles of seismic holography for diagnostics of the shallow subphotosphere, The Astrophysical Journal Supplement Series, 155, 209–225, 2004.

Lobkis, O. I. and Weaver, R. L.: On the emergence of the Green's function in the correlations of a diffuse field, Journal of the Acoustical Society of America, 110, 3011–3017, 2001.

McMechan, G. A.: Determination of source parameters by wavefield extrapolation, Geophysical Journal of the Royal Astronomical Society, 71, 613–628, 1982.

5   McMechan, G. A.: Migration by extrapolation of time-dependent boundary values, Geophysical Prospecting, 31, 413–420, 1983.

Meles, G. A., Löer, K., Ravasi, M., Curtis, A., and da Costa Filho, C. A.: Internal multiple prediction and removal using Marchenko autofocusing and seismic interferometry, Geophysics, 80, A7–A11, 2015.

Nakata, N., Gualtieri, L., and Fichtner, A.: Seismic ambient noise, Cambridge University Press, 2019.

Oren, C. and Nowack, R. L.: Seismic body-wave interferometry using noise autocorrelations for crustal structure, Geophysical Journal International, 208, 321–332, 2017.

Oristaglio, M. L.: An inverse scattering formula that uses all the data, Inverse Problems, 5, 1097–1105, 1989.

Porter, R. P.: Diffraction-limited, scalar image formation with holograms of arbitrary shape, Journal of the Optical Society of America, 60, 1051–1059, 1970.

Porter, R. P. and Devaney, A. J.: Holography and the inverse source problem, Journal of the Optical Society of America, 72, 327–330, 1982.

15   Ravasi, M., Vasconcelos, I., Kritski, A., Curtis, A., da Costa Filho, C. A., and Meles, G. A.: Target-oriented Marchenko imaging of a North Sea field, Geophysical Journal International, 205, 99–104, 2016.

Reinicke Urruticoechea, C. and Wapenaar, K.: Elastodynamic single-sided homogeneous Green's function representation: Theory and numerical examples, Wave Motion, xx, (under review), 2019.

Rickett, J. and Claerbout, J.: Acoustic daylight imaging via spectral factorization: Helioseismology and reservoir monitoring, The Leading Edge, 18, 957–960, 1999.

20   Roux, P., Sabra, K. G., Kuperman, W. A., and Roux, A.: Ambient noise cross correlation in free space: Theoretical approach, Journal of the Acoustical Society of America, 117, 79–84, 2005.

Ruigrok, E., Campman, X., and Wapenaar, K.: Basin delineation with a 40-hour passive seismic record, Bulletin of the Seismological Society of America, 102, 2165–2176, 2012.

25   Sabra, K. G., Gerstoft, P., Roux, P., Kuperman, W. A., and Fehler, M. C.: Surface wave tomography from microseisms in Southern California, Geophysical Research Letters, 32, L14 311, 2005a.

Sabra, K. G., Gerstoft, P., Roux, P., Kuperman, W. A., and Fehler, M. C.: Extracting time-domain Green's function estimates from ambient seismic noise, Geophysical Research Letters, 32, L03 310, 2005b.

Scalerandi, M., Griffa, M., and Johnson, P. A.: Robustness of computational time reversal imaging in media with elastic constant uncertainties, Journal of Applied Physics, 106, 114 911, 2009.

30   Schneider, W. A.: Integral formulation for migration in two and three dimensions, Geophysics, 43, 49–76, 1978.

Schuster, G. T.: Theory of daylight/interferometric imaging: tutorial, in: EAGE, Extended Abstracts, p. A32, 2001.

Schuster, G. T.: Seismic interferometry, Cambridge University Press, 2009.

Schuster, G. T., Yu, J., Sheng, J., and Rickett, J.: Interferometric/daylight seismic imaging, Geophysical Journal International, 157, 838–852, 2004.

35   Shapiro, N. M. and Campillo, M.: Emergence of broadband Rayleigh waves from correlations of the ambient seismic noise, Geophysical Research Letters, 31, L07 614, 2004.

Shapiro, N. M., Campillo, M., Stehly, L., and Ritzwoller, M. H.: High-resolution surface-wave tomography from ambient seismic noise, Science, 307, 1615–1618, 2005.

Slob, E., Wapenaar, K., Broggini, F., and Snieder, R.: Seismic reflector imaging using internal multiples with Marchenko-type equations, Geophysics, 79, S63–S76, 2014.

5 Snieder, R.: Extracting the Green's function from the correlation of coda waves: A derivation based on stationary phase, Physical Review E, 69, 046 610, 2004.

Staring, M., Pereira, R., Douma, H., van der Neut, J., and Wapenaar, K.: Source-receiver Marchenko redatuming on field data using an adaptive double-focusing method, Geophysics, 83, S579–S590, 2018.

Stehly, L., Campillo, M., Froment, B., and Weaver, R. L.: Reconstructing Green's function by correlation of the coda of the correlation (C^3)
10 of ambient seismic noise, Journal of Geophysical Research, 113, B11 306, 2008.

Tanter, M. and Fink, M.: Ultrafast imaging in biomedical ultrasound, IEEE Transactions on Ultrasonics, Ferroelectrics, and Frequency Control, 61, 102–119, 2014.

Tarantola, A.: Inversion of seismic reflection data in the acoustic approximation, Geophysics, 49, 1259–1266, 1984.

Ten Kroode, F.: Prediction of internal multiples, Wave Motion, 35, 315–338, 2002.

15 Tonegawa, T., Nishida, K., Watanabe, T., and Shiomi, K.: Seismic interferometry of teleseismic S-wave coda for retrieval of body waves: an application to the Philippine Sea slab underneath the Japanese Islands, Geophysical Journal International, 178, 1574–1586, 2009.

Tromp, J., Tape, C., and Liu, Q.: Seismic tomography, adjoint methods, time reversal and banana-doughnut kernels, Geophysical Journal International, 160, 195–216, 2005.

van der Neut, J. and Wapenaar, K.: Adaptive overburden elimination with the multidimensional Marchenko equation, Geophysis, 21, T265–
20 T284, 2016.

van der Neut, J., Tatanova, M., Thorbecke, J., Slob, E., and Wapenaar, K.: Deghosting, demultiple, and deblurring in controlled-source seismic interferometry, International Journal of Geophysics, 2011, 870 819, 2011.

van der Neut, J., Wapenaar, K., Thorbecke, J., and Vasconcelos, I.: Internal multiple suppression by adaptive Marchenko redatuming, in: SEG, Expanded Abstracts, pp. 4055–4059, 2014.

25 Van der Neut, J., Johnson, J. L., van Wijk, K., Singh, S., Slob, E., and Wapenaar, K.: A Marchenko equation for acoustic inverse source problems, Journal of the Acoustical Society of America, 141, 4332–4346, 2017.

van Manen, D.-J., Robertsson, J. O. A., and Curtis, A.: Modeling of wave propagation in inhomogeneous media, Physical Review Letters, 94, 164 301, 2005.

Virieux, J. and Operto, S.: An overview of full-waveform inversion in exploration geophysics, Geophysics, 74, WCC1–WCC26, 2009.

30 Wang, W. and McMechan, G. A.: Vector-based elastic reverse time migration, Geophysics, 80, S245–S258, 2015.

Wapenaar, C. P. A. and Berkhout, A. J.: Elastic wave field extrapolation, Elsevier, Amsterdam, 1989.

Wapenaar, C. P. A., Peels, G. L., Budejicky, V., and Berkhout, A. J.: Inverse extrapolation of primary seismic waves, Geophysics, 54, 853–863, 1989.

Wapenaar, K.: Retrieving the elastodynamic Green's function of an arbitrary inhomogeneous medium by cross correlation, Physical Review
35 Letters, 93, 254 301, 2004.

Wapenaar, K. and Thorbecke, J.: Review paper: Virtual sources and their responses, Part I: time-reversal acoustics and seismic interferometry, Geophysical Prospecting, 65, 1411–1429, 2017.

Wapenaar, K. and van der Neut, J.: A representation for Green's function retrieval by multidimensional deconvolution, Journal of the Acoustical Society of America, 128, EL366–EL371, 2010.

Wapenaar, K., Draganov, D., Thorbecke, J., and Fokkema, J.: Theory of acoustic daylight imaging revisited, in: SEG, Expanded Abstracts, pp. 2269–2272, 2002.

5 Wapenaar, K., Draganov, D., Snieder, R., Campman, X., and Verdel, A.: Tutorial on seismic interferometry: Part 1 - Basic principles and applications, Geophysics, 75, 75A195–75A209, 2010.

Wapenaar, K., van der Neut, J., Ruigrok, E., Draganov, D., Hunziker, J., Slob, E., Thorbecke, J., and Snieder, R.: Seismic interferometry by crosscorrelation and by multidimensional deconvolution: a systematic comparison, Geophysical Journal International, 185, 1335–1364, 2011.

10 Wapenaar, K., Thorbecke, J., van der Neut, J., Broggini, F., Slob, E., and Snieder, R.: Marchenko imaging, Geophysics, 79, WA39–WA57, 2014.

Wapenaar, K., Thorbecke, J., and van der Neut, J.: A single-sided homogeneous Green's function representation for holographic imaging, inverse scattering, time-reversal acoustics and interferometric Green's function retrieval, Geophysical Journal International, 205, 531–535, 2016a.

15 Wapenaar, K., van der Neut, J., and Slob, E.: Unified double- and single-sided homogeneous Green's function representations, Proceedings of the Royal Society A, 472, 20160 162, 2016b.

Weaver, R. L. and Lobkis, O. I.: Ultrasonics without a source: Thermal fluctuation correlations at MHz frequencies, Physical Review Letters, 87, 134 301, 2001.

Weaver, R. L. and Lobkis, O. I.: On the emergence of the Green's function in the correlations of a diffuse field: pulse-echo using thermal 20 phonons, Ultrasonics, 40, 435–439, 2002.

Weaver, R. L. and Lobkis, O. I.: Diffuse fields in open systems and the emergence of the Green's function (L), Journal of the Acoustical Society of America, 116, 2731–2734, 2004.

Weglein, A. B., Gasparotto, F. A., Carvalho, P. M., and Stolt, R. H.: An inverse-scattering series method for attenuating multiples in seismic reflection data, Geophysics, 62, 1975–1989, 1997.

25 Weglein, A. B., Hsu, S. Y., Terenghi, P., Li, X., and Stolt, R. H.: Multiple attenuation: Recent advances and the road ahead (2011), The Leading Edge, 30, 864–875, 2011.

Whitmore, N. D.: Iterative depth migration by backward time propagation, in: SEG, Expanded Abstracts, pp. 382–385, 1983.

Wiggins, J. W.: Kirchhoff integral extrapolation and migration of nonplanar data, Geophysics, 49, 1239–1248, 1984.

Zhang, L., Thorbecke, J., Wapenaar, K., and Slob, E.: Transmission compensated primary reflection retrieval in data domain and conse-30 quences for imaging, Geophysics, 84, (under review), 2019.

Zhang, Y. and Sun, J.: Practical issues in reverse time migration: true amplitude gathers, noise removal and harmonic source encoding, First Break, 27, 53–59, 2009.

Zheng, Y., He, Y., and Fehler, M. C.: Crosscorrelation kernels in acoustic Green's function retrieval by wavefield correlation for point sources on a plane and a sphere, Geophysical Journal International, 184, 853–859, 2011.